Electronic Supplementary Material (ESI) for Journal of Materials Chemistry A.

Supporting Information for

Sequential precipitation induced interdiffusion: A general strategy to synthesize microtubular materials for high performance lithium-ion battery electrodes

Fei Chen,[†] Weixin Zhang,*[†] Junrui Fu,[†] Zeheng Yang,[†] Xiaoming Fan,[†] Weibo Zhang,[†] Zhangxian Chen,[†] Mengqiu Huang,[†] and Shihe Yang*[‡]

[†]*School of Chemistry and Chemical Engineering, Hefei University of Technology, Hefei, Anhui 230009, P. R. China*

‡Guangdong Key Lab of Nano-Micro Material Research, School of Chemical Biology and Biotechnology, Shenzhen Graduate School, Peking University, Shenzhen 518055, P. R. China

AUTHOR INFORMATION

Corresponding Authors

***E-mail: wxzhang@hfut.edu.cn (Weixin Zhang)**

***E-mail: yangsh@pkusz.edu.cn (Shihe Yang)**

Experimental section

In this work, the required reagents were purchased from Shanghai Chemical Reagent Co. (China) and used as received without further purification.

Preparation of $LiNi_{0.8}Co_{0.1}Mn_{0.1}O_2$ cathode material

In a typical synthesis, 20 mL of 0.1 M $Co(CH_3COO)_2·4H_2O$ and 40 mL of 0.75 M $H_2C_2O_4·2H_2O$ were first mixed with magnetic stirring for 3 h to get a pink turbid liquid. Then, 20 mL of 0.8 M $Ni(CH_3COO)_2·4H_2O$ and 20 mL of 0.1 M $Mn(CH_3COO)_2·4H_2O$ were put into the pink turbid liquid and stirred for 8 h to form suspension. The suspension was evaporated in air for 12 h at 70 °C to get the $MC_2O_4·xH_2O$ (M= Ni, Co and Mn) powder. The as-prepared $MC_2O_4·xH_2O$ precursors were mixed with CH_3COOLi with a molar ratio of 1:1.05, then calcined at 480 ºC for 5 h (heating rate: 4.0 ºC min^{-1}) and at 750 ºC for 15 h (heating rate: 4.0 ºC min^{-1}) in flowing pure oxygen to get the final $LiNi_{0.8}Co_{0.1}Mn_{0.1}O_2$ microtubes (named as LNCM811-MTs).

For comparison, $LiNi_{0.8}Co_{0.1}Mn_{0.1}O_2$ microparticles were prepared based on a conventional co-precipitation reaction. 20 mL of 0.8 M $Ni(CH_3COO)_2·4H_2O$, 20 mL of 0.1 M $Co(CH_3COO)_2·4H_2O$ and 20 mL of 0.1 M $Mn(CH_3COO)_2·4H_2O$ solutions were mixed and added in 40 mL of 0.75 M $H_2C_2O_4·2H_2O$ solution for co-precipitation preparation of $MC_2O_4·xH_2O$ (M= Ni, Co and Mn) as precursor. The subsequent implanting Li and post-heat treatment procedures eith the precursor were the same as the above mentioned to get the $LiNi_{0.8}Co_{0.1}Mn_{0.1}O_2$ particles (named as LNCM811-MPs).

Preparation of $0.5Li_2MnO_3·0.5LiNi_{1/3}Co_{1/3}Mn_{1/3}O_2$ ($Li_{1.2}Ni_{0.13}Co_{0.13}Mn_{0.54}O_2$) cathode material

In a typical synthesis process, 10 mL of $Co(CH_3COO)_2·4H_2O$ solution (0.1 M) was firstly added to 20 mL of $H_2C_2O_4·2H_2O$ solution (1 M) with magnetic stirring for 3 h to form suspension A. Then, 10 mL of $Ni(CH_3COO)·4H_2O$ solution (0.1 M) and 10 mL of $Mn(CH_3COO)_2·4H_2O$ solution (0.4 M) were mixed together to obtain solution B, which was poured into suspension A with constant magnetic stirring for 8 h to form suspension C. The suspension C was evaporated in air for 12 h at 70 °C to get the $MC_2O_4·xH_2O$ (M= Ni, Co and Mn) powder. After being ground with an excess of CH_3COOLi (excessive 5 % for compensating the loss of Li during calcination), the mixture was calcined in air at 450 °C for 8 h and 850 °C for 15 h with a heating rate of 4 °C min^{-1} to obtain Li-rich $Li_{1.2}Ni_{0.13}Co_{0.13}Mn_{0.54}O_2$ microtubes (named as LR-MTs).

For comparison, Li-rich $Li_{1.2}Ni_{0.13}Co_{0.13}Mn_{0.54}O_2$ microsized particles (named as LR-MPs) were prepared based on a conventional co-precipitation reaction. $Ni(CH_3COO)_2·4H_2O$ (0.1 M), $Co(CH_3COO)_2·4H_2O$ (0.1 M) and $Mn(CH_3COO)_2·4H_2O$ (0.4 M) solutions with 10 mL of each were mixed together and then added in 20 mL of $H_2C_2O_4$ solution (1 M). The subsequent Li implanting and calcination procedures were the same as the ones mentioned above.

Preparation of $Li_{1.2}Ni_{0.13}Co_{0.10}Mn_{0.54}Fe_{0.03}O_2$ cathode material

In a typical synthesis process of $Li_{1.2}Ni_{0.13}Co_{0.10}Mn_{0.54}Fe_{0.03}O_2$, 7.7 mL of $Co(CH_3COO)_2·4H_2O$ solution (0.1 M) was firstly added to 20 mL of $H_2C_2O_4·2H_2O$ solution (1 M) with magnetic stirring for 3 h to form suspension A. Then, 2.3 mL of $FeSO_4·7H_2O$ (0.1 M), 10 mL of $Ni(CH_3COO)·4H_2O$ solution (0.1 M) and 10 mL of $Mn(CH_3COO)_2·4H_2O$ solution (0.4 M) were mixed together to obtain solution B, which was poured into suspension A with constant magnetic stirring for 8 h to form suspension C. The suspension C was evaporated in air for 12 h at 70 °C to get the $MC_2O_4·xH_2O$ (M= Ni, Co, Mn and Fe) powder. After being ground with an excess of CH_3COOLi (excessive 5 % for compensating the loss of Li during calcination), the mixture was calcined in air at 450 °C for 8 h and 850 °C for 15 h with a heating rate of 4 °C min^{-1} to obtain Li-rich $Li_{1.2}Ni_{0.13}Co_{0.10}Mn_{0.54}Fe_{0.03}O_2$ microtubes.

Preparation of $Li_{1.2}Ni_{0.10}Co_{0.13}Mn_{0.54}Cu_{0.03}O_2$ cathode material

In a typical synthesis process of $Li_{1.2}Ni_{0.10}Co_{0.13}Mn_{0.54}Cu_{0.03}O_2$, 7.7 mL of $Co(CH_3COO)_2·4H_2O$ solution (0.1 M) was firstly added to 20 mL of $H_2C_2O_4·2H_2O$ solution (1 M) with magnetic stirring for 3 h to form suspension A. Then, 2.3 mL of $Cu(CH_3COO)_2·2H_2O$ (0.1 M), 10 mL of $Ni(CH_3COO)·4H_2O$ solution (0.1 M) and 10 mL of $Mn(CH_3COO)_2·4H_2O$ solution (0.4 M) were mixed together to obtain solution B, which was poured into suspension A with constant magnetic stirring for 8 h to form suspension C. The suspension C was evaporated in air for 12 h at 70 °C to get the $MC_2O_4·xH_2O$ (M= Ni, Co, Mn and Cu) powder. After being ground with an excess of CH_3COOLi (excessive 5 % for compensating the loss of Li during calcination), the mixture was calcined in air at 450 °C for 8 h and 850 °C for 15 h with a heating rate of 4 °C min^{-1} to obtain Li-rich $Li_{1.2}Ni_{0.10}Co_{0.13}Mn_{0.54}Cu_{0.03}O_2$ microtubes.

Preparation of $LiNi_{0.5}Co_{0.2}Mn_{0.3}O_2$ cathode material

In a typical synthesis process of $LiNi_{0.5}Co_{0.2}Mn_{0.3}O_2$, 20 mL of $Co(CH_3COO)_2·4H_2O$ solution (0.1 M) was firstly added to 20 mL of $H_2C_2O_4·2H_2O$ solution (1 M) under magnetic stirring for 3 h to form suspension A. Then, 20 mL of $Ni(CH_3COO)·4H_2O$ solution (0.25 M) and 20 mL of $Mn(CH_3COO)_2·4H_2O$ solution (0.15 M) were mixed together to obtain solution B, which was poured into suspension A with constant magnetic stirring for 8 h to form suspension C. The suspension C was evaporated in air for 12 h at 70 °C to get the $MC_2O_4·xH_2O$ (M= Ni, Co and Mn) powder. After being ground with an excess of CH_3COOLi (excessive 5 % for compensating the loss of Li during calcination), the mixture was calcined in air at 450 °C for 8 h and 850 °C for 15 h with a heating rate of 4 °C min^{-1} to obtain layered $LiNi_{0.5}Co_{0.2}Mn_{0.3}O_2$ microtube products (named as LNCM523).

Preparation of $LiNi_{0.6}Co_{0.2}Mn_{0.2}O_2$ cathode material

In a typical synthesis process of $LiNi_{0.6}Co_{0.2}Mn_{0.2}O_2$, 20 mL of $Co(CH_3COO)_2·4H_2O$ solution (0.1 M) was firstly added to 20 mL of $H_2C_2O_4·2H_2O$ solution (1 M) under magnetic stirring for 3 h to form suspension A. Then, 20 mL of $Ni(CH_3COO)·4H_2O$ solution (0.3 M) and 20 mL of $Mn(CH_3COO)_2·4H_2O$ solution (0.1 M) were mixed together to obtain solution B, which was poured into suspension A with constant magnetic stirring for 8 h to form suspension C. The suspension C was evaporated in air for 12 h at 70 °C to get the $MC_2O_4{\cdot}xH_2O$ (M= Ni, Co and Mn) powder. After being ground with an excess of CH_3COOLi (excessive 5 % for compensating the loss of Li during calcination), the mixture was calcined in air at 450 °C for 6 h and 850 °C for 15 h with a heating rate of 4 °C min^{-1} to obtain layered $LiNi_{0.6}Co_{0.2}Mn_{0.2}O_2$ microtube products (named as LNCM622).

Preparation of the oxalate precursor for $LiNi_{1/3}Co_{1/3}Mn_{1/3}O_2$ cathode material

In a typical synthesis process of $LiNi_{1/3}Co_{1/3}Mn_{1/3}O_2$, 20 mL of $Co(CH_3COO)_2{\cdot}4H_2O$ solution (0.1 M) was firstly added to 20 mL of $H_2C_2O_4{\cdot}2H_2O$ solution (0.9 M) under magnetic stirring for 3 h to form suspension A. Then, 20 mL of $Ni(CH_3COO){\cdot}4H_2O$ solution (0.1 M) and 20 mL of $Mn(CH_3COO)_2{\cdot}4H_2O$ solution (0.1 M) were mixed together to obtain solution B, which was poured into suspension A with constant magnetic stirring for 8 h to form suspension C. The suspension C was evaporated in air for 12 h at 70 °C to get the $MC_2O_4{\cdot}xH_2O$ (M= Ni, Co and Mn) powder.

Preparation of oxalate precursor for $LiNi_{0.7}Co_{0.1}Mn_{0.2}O_2$ cathode material

In a typical synthesis process of $LiNi_{0.7}Co_{0.1}Mn_{0.2}O_2$, 20 mL of $Co(CH_3COO)_2{\cdot}4H_2O$ solution (0.1 M) was firstly added to 20 mL of $H_2C_2O_4{\cdot}2H_2O$ solution (1 M) under magnetic stirring for 3 h to form suspension A. Then, 20 mL of $Ni(CH_3COO){\cdot}4H_2O$ solution (0.7 M) and 20 mL of $Mn(CH_3COO)_2{\cdot}4H_2O$ solution (0.2 M) were mixed together to obtain solution B, which was poured into suspension A with constant magnetic stirring for 8 h to form suspension C. The suspension C was evaporated in air for 12 h at 70 °C to get the $MC_2O_4{\cdot}xH_2O$ (M= Ni, Co and Mn) powder.

Preparation of $NiCo_2O_4$ anode material

In a typical synthesis process of $NiCo_2O_4$, 20 mL of $Co(CH_3COO)_2{\cdot}4H_2O$ solution (0.2 M) was firstly added to 20 mL of $H_2C_2O_4{\cdot}2H_2O$ solution (0.9 M) under magnetic stirring for 3 h to form suspension A. Then, 20 mL of $Ni(CH_3COO){\cdot}4H_2O$ solution (0.1 M) was poured into suspension A with constant magnetic stirring for 6 h to form suspension B. The suspension B was evaporated in air for 12 h at 70 °C to get the $MC_2O_4{\cdot}xH_2O$ (M= Ni, Co) powder. The mixture was calcined in air at 450 °C for 2 h with a heating rate of 2 °C min^{-1} to obtain $NiCo_2O_4$ nanotube products.

Preparation of $ZnCo_2O_4$ anode material

In a typical synthesis process of $ZnCo_2O_4$, 20 mL of $Co(CH_3COO)_2{\cdot}4H_2O$ solution (0.2 M) was firstly added to 20 mL of $H_2C_2O_4{\cdot}2H_2O$ solution (0.9 M) under magnetic stirring for 3 h to form suspension A. Then, 20 mL of $Zn(CH_3COO){\cdot}4H_2O$ solution (0.1 M) was poured into suspension A with constant magnetic stirring for 6 h to form suspension B. The suspension B was evaporated in air for 12 h at 70 °C to get the $MC_2O_4{\cdot}xH_2O$ (M= Zn, Co) powder. The mixture was calcined in air at 550 °C for 2 h with a heating rate of 2 °C min^{-1} to obtain $ZnCo_2O_4$ nanotube products.

Preparation of $MC_2O_4{\cdot}xH_2O$ (M= Ni, Co and Mn) precursor for $Li_{1.2}Ni_{0.13}Co_{0.13}Mn_{0.54}O_2$ in water/ethanol mixed solvent

In a typical sequential precipitation process, 50 mL of $Mn(CH_3COO)_2 \cdot 4H_2O$ solution (0.4 M, H_2O: EtOH=1:4) was firstly added to 50 mL of $H_2C_2O_4 \cdot 2H_2O$ solution (1 M, H_2O: EtOH=1:4) under magnetic stirring for 1 h to form suspension A. Then, 50 mL of $Ni(CH_3COO) \cdot 4H_2O$ solution (0.1 M, H_2O: EtOH=1:4) and 50 mL of $Co(CH_3COO)_2 \cdot 4H_2O$ solution (0.1 M, H_2O:EtOH=1:4) were mixed together to obtain solution B, which was poured into suspension A with constant magnetic stirring for 8 h to form suspension C. The suspension C was evaporated in air for 12 h at 70 °C to get the $MC_2O_4 \cdot xH_2O$ (M= Ni, Co and Mn) powder.

For comparison, in a typical co-precipitation process, 50 mL of 0.4 M $Mn(CH_3COO)_2 \cdot 4H_2O$, 50 mL of 0.1 M $Ni(CH_3COO)_2 \cdot 4H_2O$ and 50 mL of 0.1 M $Co(CH_3COO)_2 \cdot 4H_2O$ solution (H_2O:EtOH=1:4) were mixed and added to 50 mL of $H_2C_2O_4 \cdot 2H_2O$ solution (1 M, H_2O: EtOH=1:4) under magnetic stirring for 8 h to get the suspension, which was evaporated in air for 12 h at 70 °C to get the $MC_2O_4 \cdot xH_2O$ (M= Ni, Co and Mn) powder.

Preparation of $Na_{0.56}Ni_{0.13}Co_{0.13}Mn_{0.54}O_2$ cathode material

In a typical synthesis process, 10 mL of $Co(CH_3COO)_2 \cdot 4H_2O$ solution (0.1 M) was firstly added to 20 mL of $H_2C_2O_4 \cdot 2H_2O$ solution (1 M) with magnetic stirring for 3 h to form suspension A. Then, 10 mL of $Ni(CH_3COO) \cdot 4H_2O$ solution (0.1 M) and 10 mL of $Mn(CH_3COO)_2 \cdot 4H_2O$ solution (0.4 M) were mixed together to obtain solution B, which was poured into suspension A with constant magnetic stirring for 8 h to form suspension C. The suspension C was evaporated in air for 12 h at 70 °C to get the $MC_2O_4 \cdot xH_2O$ (M= Ni, Co and Mn) powder. After being ground with an excess of CH_3COONa (excessive 5 % for compensating the loss of Na during calcination), the mixture was calcined in air at 450 °C for 6 h and 800 °C for 15 h with a heating rate of 4 °C min^{-1} to obtain $Na_{0.56}Ni_{0.13}Co_{0.13}Mn_{0.54}O_2$ microtubes.

Material characterizations

The composition and structure of the as-prepared samples were examined by X-ray diffraction (XRD) on a Shimadzu D/max-γB X-ray diffractometer using a Cu Kα radiation source (λ= 0.154178 nm) operated at 40 kV and 80 mA. Field-emission scanning electron microscopy (FESEM) (Hitachi SU8020) measurements were carried out at an acceleration voltage of 5 kV, respectively. Transmission electron microscopy (TEM) images of the samples were taken on a Hitachi H-800 operated at accelerating voltage of 200 kV. HRTEM images and elemental mapping of the samples were taken on a field-emission transmission electron microscope (JEOL-2010). The samples were also examined by energy dispersive spectroscopy (EDS). The results of N_2 adsorption-desorption isotherms were obtained on a Quantachrome NOVA 2200e surface area and pore-size analyzer at liquid nitrogen temperature. The specific surface area of the samples was calculated by following the multipoint Brunauer-Emmett-Teller (BET) procedure, and average pore diameters were determined by the Barrett-Joyner-Halenda (BJH) method.

Electrochemical measurements

The LNCM cathodes were prepared by mixing 80 wt% active material, 10 wt% acetylene black (Beijing Chemical Reagents Corporation, China) and 10 wt% polyvinylidene fluoride (PVDF, Shanghai Chemical Reagents Corporation, China) as a binder in a solvent of N-methyl-2-pyrrolidone (NMP, Shanghai Chemical Reagents Corporation, China) to form a homogeneous slurry. The mixed slurry was cast onto aluminum foil with the slurry thickness controlled. After the evaporation of the solvent at 65 °C for 2 h in air, the cathode was roll-pressed and cut into pellets of required size for coin-cell fabrication, the pellets were further dried under high vacuum at 120 °C for 5 h. Lithium foil (Energy Lithium Limited Corporation, China) was used as counter electrode. The liquid electrolyte utilized was 1 mol L^{-1} $LiPF_6$ in a 1:1 (volume) mixture of ethylene carbonate (EC) and dimethyl carbonate (DMC), and the separator was a polypropylene membrane with micro-pores (Celgard 2400). The coin-type cells (CR2032) were assembled in an Ar-filled dry glove box.

The galvanostatic charge-discharge experiment was conducted using a battery testing system (BTS-5V/10mA, Neware Technology Limited Corporation, China) from 2.8 to 4.3 V (versus Li^+/Li). The cyclic voltammetry (CV) curves were obtained using an electrochemical workstation (CHI-660E, Shanghai Chenhua Instrument Corporation, China) at scan rate of 0.1 mV s^{-1} from 2.8 to 4.3 V (versus Li/Li^+). Electrochemical impedance spectroscopic (EIS) measurements) was also performed on the electrochemical workstation and the excitation potential applied to the cells was 5 mV and the frequency ranged from 100 kHz to 10 mHz.

The $Na_{0.56}Ni_{0.13}Co_{0.13}Mn_{0.54}O_2$ cathode material were prepared by mixing 70 wt% active material, 20 wt% acetylene black (Beijing Chemical Reagents Corporation, China) and 10 wt% polyvinylidene fluoride (PVDF, Shanghai Chemical Reagents Corporation, China) as a binder in a solvent of N-methyl-2-pyrrolidone (NMP, Shanghai Chemical Reagents Corporation, China) to form a homogeneous slurry. The mixed slurry was cast onto aluminum foil with the slurry thickness controlled. After the evaporation of the solvent at 65 °C for 2 h in air, the cathode was roll-pressed and cut into pellets of required size for coin-cell fabrication, the pellets were further dried under high vacuum at 120 °C for 5 h. Sodium foil with diameter of 14 mm (sodium metal disk pressed on a stainless steel current collector) was used as counter electrode. The electrodes were separated by glass fiber disks, which are soaked with a 1 M solution of $NaPF_6$ in an ethylene carbonate (EC)/diethylene carbonate (DEC). The coin-type cells (CR2032) were assembled in an Ar-filled dry glove box. The galvanostatic charge-discharge experiment was conducted using a battery testing system (BTS-5V/10mA, Neware Technology Limited Corporation, China) from 1.5 to 4.3 V (versus Na^+/Na).

The loading mass of active material on the electrodes:

The cathode electrode was prepared by mixing 80 wt% active material, 10 wt% acetylene black and 10 wt% polyvinylidene fluoride. We chose $LiNi_{0.8}Co_{0.1}Mn_{0.1}O_2$ as a typical representative of cathode material to illustrate the weight of loading mass of active material, the total weight of the electrode is about 7.95 mg, and the weight of aluminum foil acted as collector is 4.64 mg. So the loading mass of the active material is about 2.65 mg by calculation (loading mass m=(7.95-4.64)*0.8=2.65). The loading mass of other cathode material is close to that of $LiNi_{0.8}Co_{0.1}Mn_{0.1}O_2$.

The $NiCo_2O_4$ anode electrode were prepared by mixing 70 wt% active material, 20 wt% acetylene black and 10 wt% polyvinylidene fluoride. The total weight of the electrode is about 12.30 mg, the weight of copper foil acted as collector is 9.90 mg. So the loading mass of the active material is about 1.68 mg by calculation (loading mass m=(12.30-9.90)*0.7=1.68).

Fig. S1

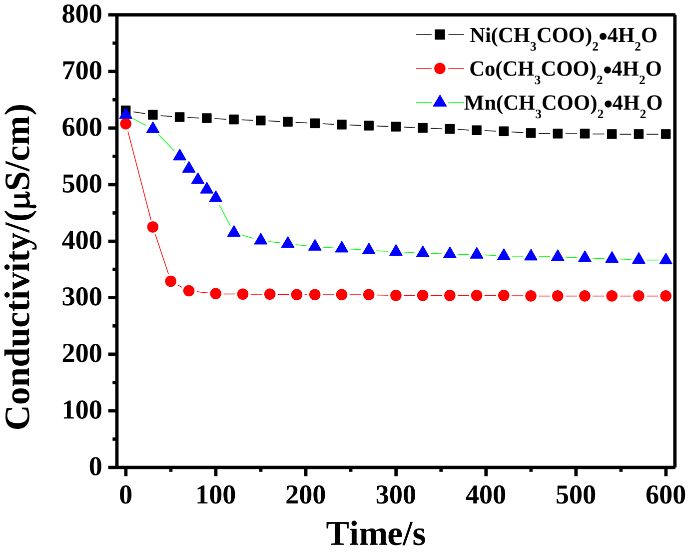

Fig. S1. The aqueous solution ionic conductivity change with time when $Mn(CH_3COO)_2 \cdot 4H_2O$, $Ni(CH_3COO)_2 \cdot 4H_2O$ or $Co(CH_3COO)_2 \cdot 4H_2O$ solution reacts with oxalic acid, respectively.

In a typical process, 20 mL of $Mn(CH_3COO)_2 \cdot 4H_2O$, $Ni(CH_3COO)_2 \cdot 4H_2O$ or $Co(CH_3COO)_2 \cdot 4H_2O$ solution (0.05 M) was added to 20 mL of $H_2C_2O_4 \cdot 2H_2O$ solution (1 M) under magnetic stirring and the ionic conductivity change with time was recorded. The ionic conductivity change (Fig. S1) with time shows that it takes about 53 s for the fast decrease from 610 μS/cm to 310 μS/cm in $Co(CH_3COO)_2 \cdot 4H_2O$ solution, 145 s for the decrease from 620 μS/cm to 405 μS/cm in $Mn(CH_3COO)_2 \cdot 4H_2O$ solution while the ionic conductivity of $Ni(CH_3COO)_2 \cdot 4H_2O$ decrease slowly. The results indicate that the $CoC_2O_4 \cdot 4H_2O$ has the biggest precipitation reaction rate and $NiC_2O_4 \cdot 2H_2O$ has the least.

Fig. S2

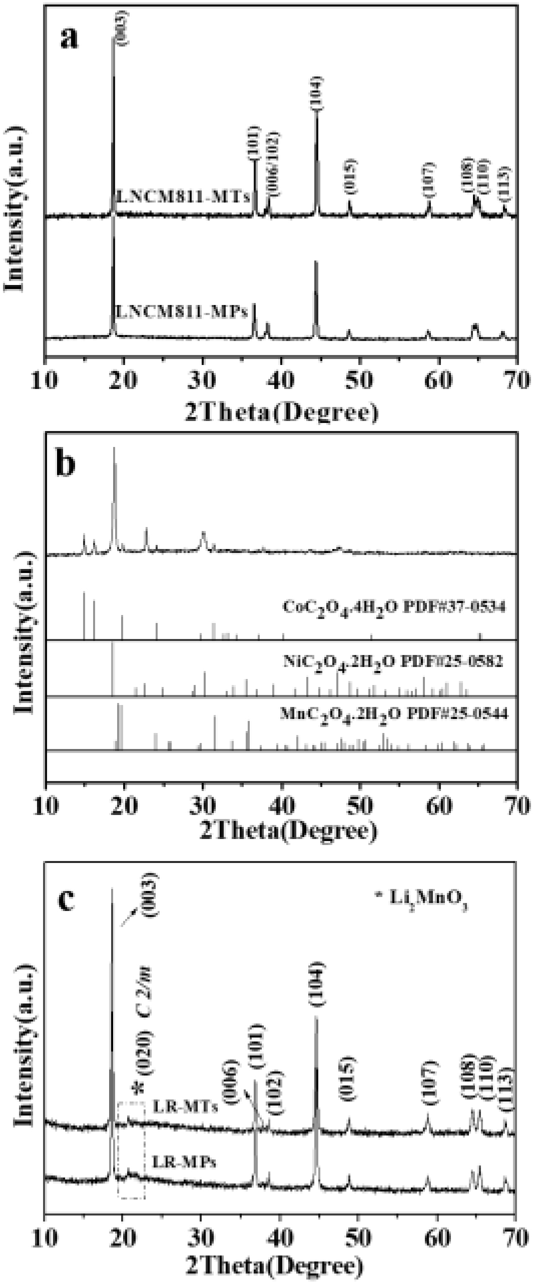

Fig. S2. (a) XRD patterns of $LiNi_{0.8}Co_{0.1}Mn_{0.1}O_2$ microtubes (LNCM811-MTs) and microparticles (LNCM811-MPs) through post-heat treatment of $MC_2O_4{\cdot}xH_2O$ (M= Ni, Co and Mn) precursor with subsequent lithium impregnation and annealing in flowing oxygen atmosphere. (b) XRD patterns of $MC_2O_4{\cdot}xH_2O$ (M=Ni, Co and Mn) precursor for $LiNi_{0.8}Co_{0.1}Mn_{0.1}O_2$ microtubes prepared by sequential precipitation with reaction time of 3 h at the first step and 8 h at the second step. (c) XRD patterns of

$Li_{1.2}Ni_{0.13}Co_{0.13}Mn_{0.54}O_2$ microtubes (LR-MTs) and microparticles (LR-MPs) through post-heat treatment of $MC_2O_4·xH_2O$ (M= Ni, Co and Mn) precursor by subsequent lithium impregnation and annealing in air.

The phase and composition of LNCM811-MTs were examined by XRD patterns (Fig. S2a). All the diffraction peaks of LNCM811-MTs can be indexed to a typical α-$NaFeO_2$ layered structure with a space group of $R\bar{3}m$, and no obvious impurity peaks were observed. The peak splitting of (006)/(102) and (108)/(110) of LNCM811-MTs are stronger than those of LNCM811-MPs, which implies the higher ordered layered hexagonal structure of LNCM811-MTs with higher order. The detailed information was described in Table S2. The XRD pattern in Fig. S2b indicates that the precursor $MC_2O_4·xH_2O$ (M= Ni, Co and Mn) is composed of $NiC_2O_4·2H_2O$ (JCPDS No. 25-0582), $CoC_2O_4·4H_2O$ (JCPDS No. 37-0534) and $MnC_2O_4·2H_2O$ (JCPDS No. 25-0544). Fig. S2c shows the XRD patterns of both LR-MTs and LR-MPs. All the diffraction peaks can be indexed to the α-$NaFeO_2$ type layered structure with a space group of $R\bar{3}m$, and no other diffraction peaks of impurities can be observed in the patterns. The splits of (006)/(102) and (108)/(110) pairs can be clearly observed in the XRD patterns, which indicates the samples have a well-crystallined layered structure. The weak peaks located at $2θ=20–25^o$ can be attributed to the component of Li_2MnO_3 (C/2m space group). The integrated intensity ratio of the (003) to (104) peaks in the XRD patterns indicates the extent of cation mixing and the value greater than 1.2 reflects a low cation disorder of Li^+ and Ni^{2+}.

Fig. S3

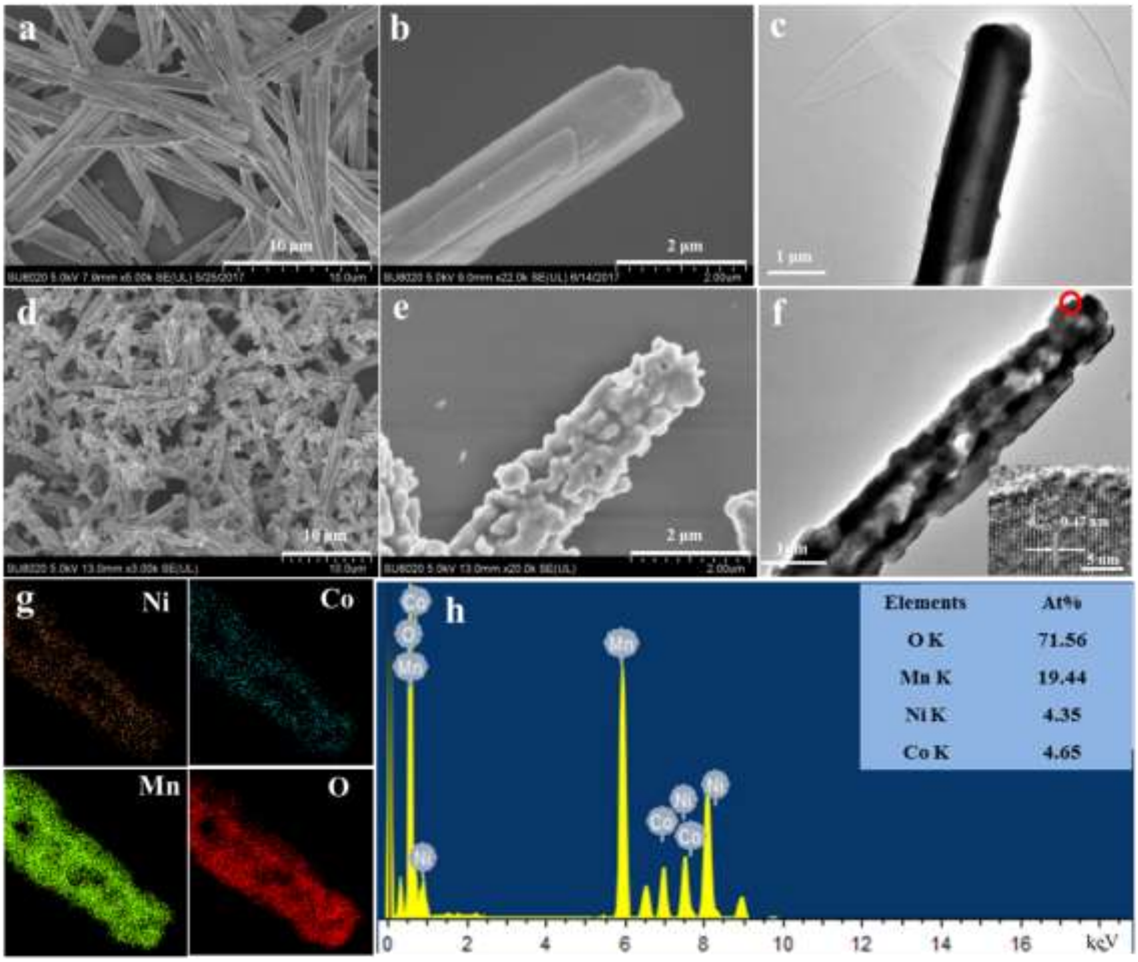

Fig. S3. (a, b) FESEM images of the oxalate precursor. (c) High resolution TEM image of the oxalate precursor. (d, e) FESEM images of LR-MTs. (f) High resolution TEM image of the LR-MTs; inset in (f): HRTEM images in the circled region on the LR-MTs. (g) EDS elemental mappings (Ni, Co, Mn and O) and (h) EDS spectrum of a single microtube of LR-MTs.

FESEM and TEM images in Fig. S3 show the hollow structure of the metal oxalate precursor and LR-MTs are composed of large scale of microrods. The metal oxalate precursor microrods display diameters of 1-2 μm and lengths of 10-20 μm (Fig. S3a and b) and the hollow structure is confirmed by the TEM image (Fig. S3c). The derived LR-MTs product (Fig. S3d, e and f) retains almost consistent hollow structure and physical dimension with those of the oxalate precursor. The TEM image of the LR-MTs (Fig. S3f) shows that they are assembly of nanoparticles with size of 100-300 nm, and void spaces can be observed on the walls, which agrees well with the FESEM images. The HRTEM image (inset in Fig. S3f) shows the characteristic plane of the layered structure of lithium-rich materials and the interplanar distance of 0.47 nm agrees well with the (003) plane of LR-MTs. EDS elemental mappings (Fig. S3g) indicate uniform distribution of Ni, Co, Mn and O elements in the LR-MTs along the axial direction with hollow interior and their element ratio of 1:1.07:4.47 (Fig. S3h) is close to the theoretical ratio of the $Li_{1.2}Ni_{0.13}Co_{0.13}Mn_{0.54}O_2$ (Ni:Co:Mn=1:1:4).

Fig. S4

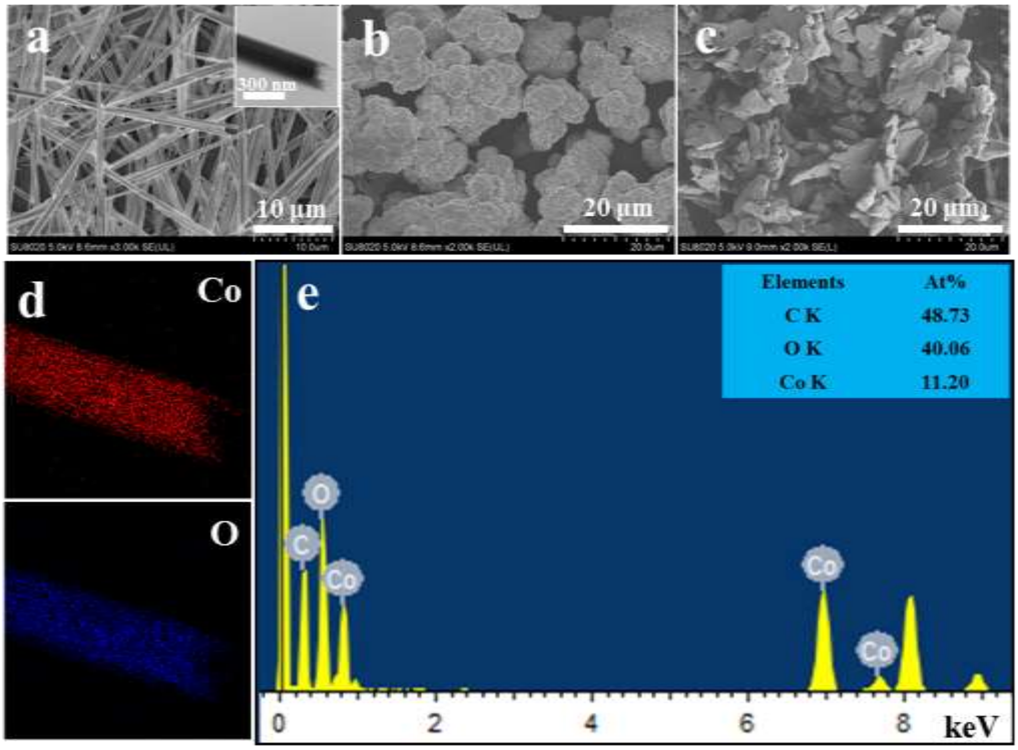

Fig. S4. FESEM images of single metal oxalate samples. (a) $CoC_2O_4{\cdot}xH_2O$, (b) $NiC_2O_4{\cdot}xH_2O$ and (c) $MnC_2O_4{\cdot}xH_2O$. Inset in (a): High resolution TEM image of $CoC_2O_4{\cdot}xH_2O$. (d) EDS elemental mappings and (e) EDS spectrum of the $CoC_2O_4{\cdot}xH_2O$.

To investigate the possible formation mechanism, individual precipitation of single metal oxalate was conducted separately. The three transition metal oxalates display different morphology, respectively (Fig. S4). $CoC_2O_4{\cdot}$exists in nanorods, $NiC_2O_4{\cdot}xH_2O$ exists in irregular micro-sized particles and $MnC_2O_4{\cdot}xH_2O$ in microplates. The $CoC_2O_4{\cdot}xH_2O$ nanorod was further analysed by the EDS elemental mappings and EDS spectrum.

Fig. S5

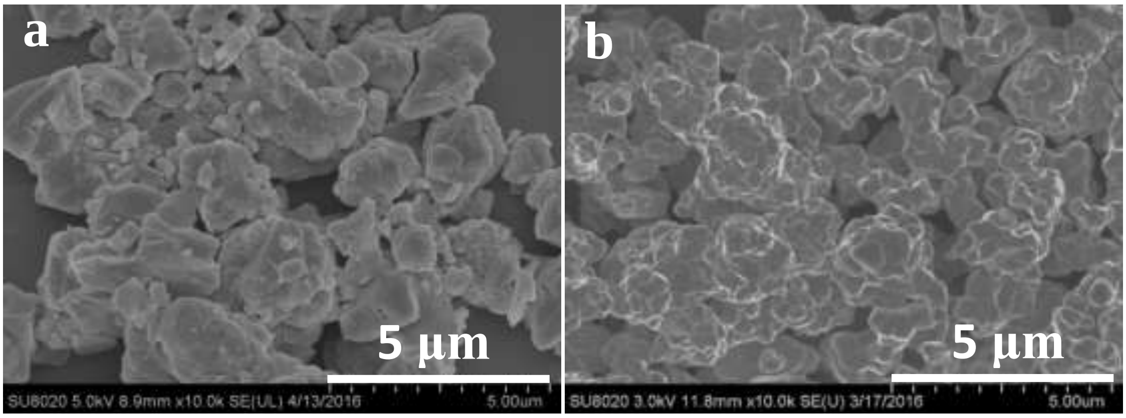

Fig. S5. FESEM images of (a) $MC_2O_4 \cdot xH_2O$ (M=Ni, Co and Mn) precursor and (b) LNCM811-MPs product prepared via a conventional co-precipitation method.

$LiNi_{0.8}Co_{0.1}Mn_{0.1}O_2$ microparticles (LNCM811-MPs) were prepared via a conventional co-precipitation (the three metal acetate solutions mixed with $H_2C_2O_4$ solution simultaneously) followed by identical procedures of lithium mixing and post-heat treatment. They exist in irregular and microsized particle morphology (Fig. S5).

Fig. S6

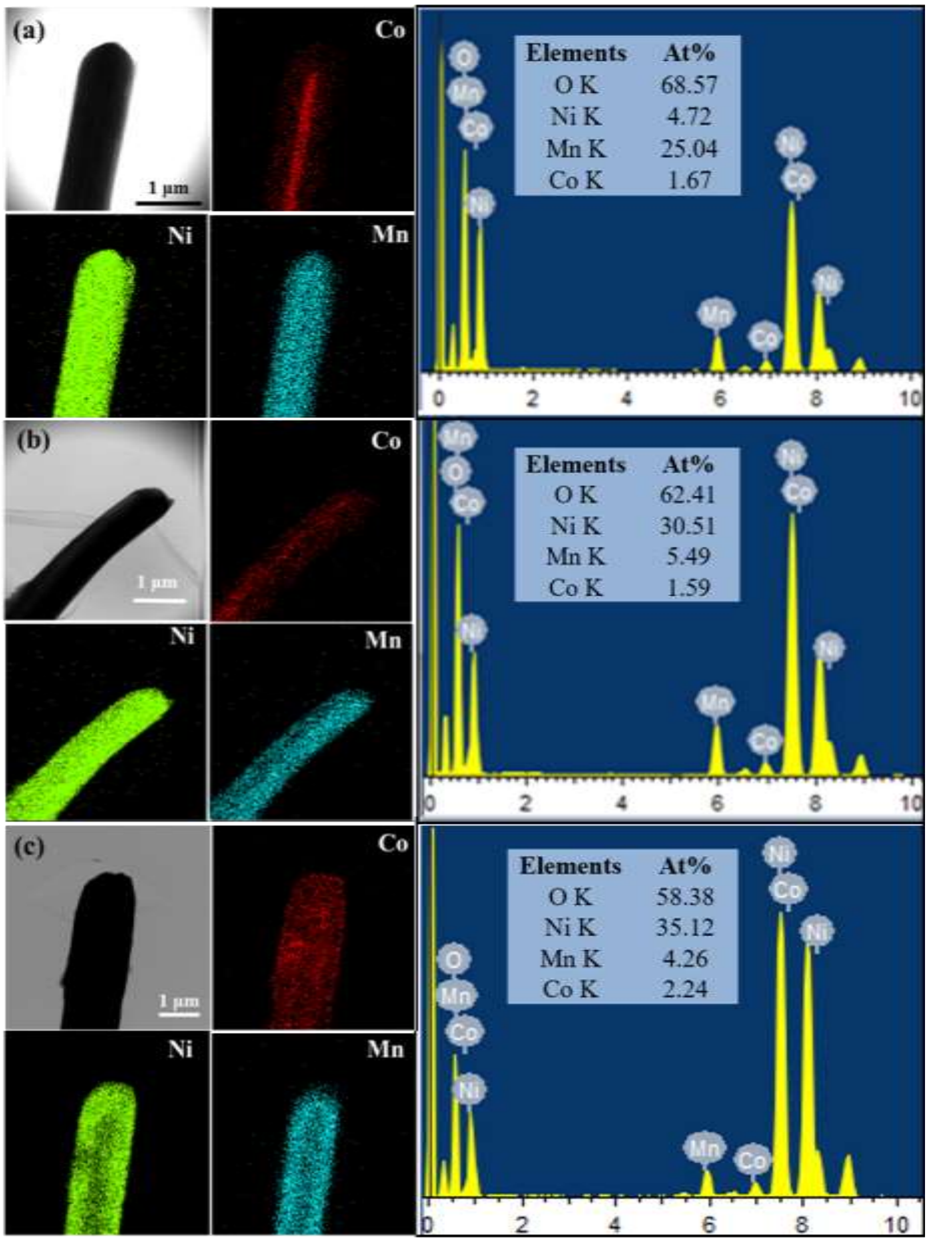

Fig. S6. EDS elemental mappings and corresponding EDS spectra of the $MC_2O_4{\cdot}xH_2O$ (M= Ni, Co and Mn) precursors for $LiNi_{0.8}Co_{0.1}Mn_{0.1}O_2$ microtubes with different reaction time at the second step: (a) 10 min, (b) 1 h and (c) 8 h.

Fig. S6 shows the EDS elemental mappings of the $MC_2O_4{\cdot}xH_2O$ (M= Ni, Co and Mn) precursor at different reaction time of 10 min, 1 h and 8 h at the second precipitation step, respectively. At the reaction time of 10 min, the diameter of the precipitate is about 500 nm composed of CoC_2O_4 core and NiC_2O_4/MnC_2O_4 shell (Fig. S6a). At 1 h, the rod grows to about 800 nm in diameter and the CoC_2O_4 core diffuses outward due to the non-equilibrium mass interdiffusion during the ripening process, but still with cobalt element distribution higher in the center than in the shell (Fig. S6b). When the reaction time comes to 8 h, the non-equilibrium interdiffusion induced by their crystallinity difference leads to the hollow structure. The tubular structure with a diameter of about 1.2 μm is formed and the nickel, cobalt and manganese elements are uniformly distributed on the whole microtube due to element migration during the ripening process (Fig. S6c). The EDS spectra show the corresponding atomic ratio variation of nickel, cobalt and manganese elements with different reaction time at the second step.

Fig. S7

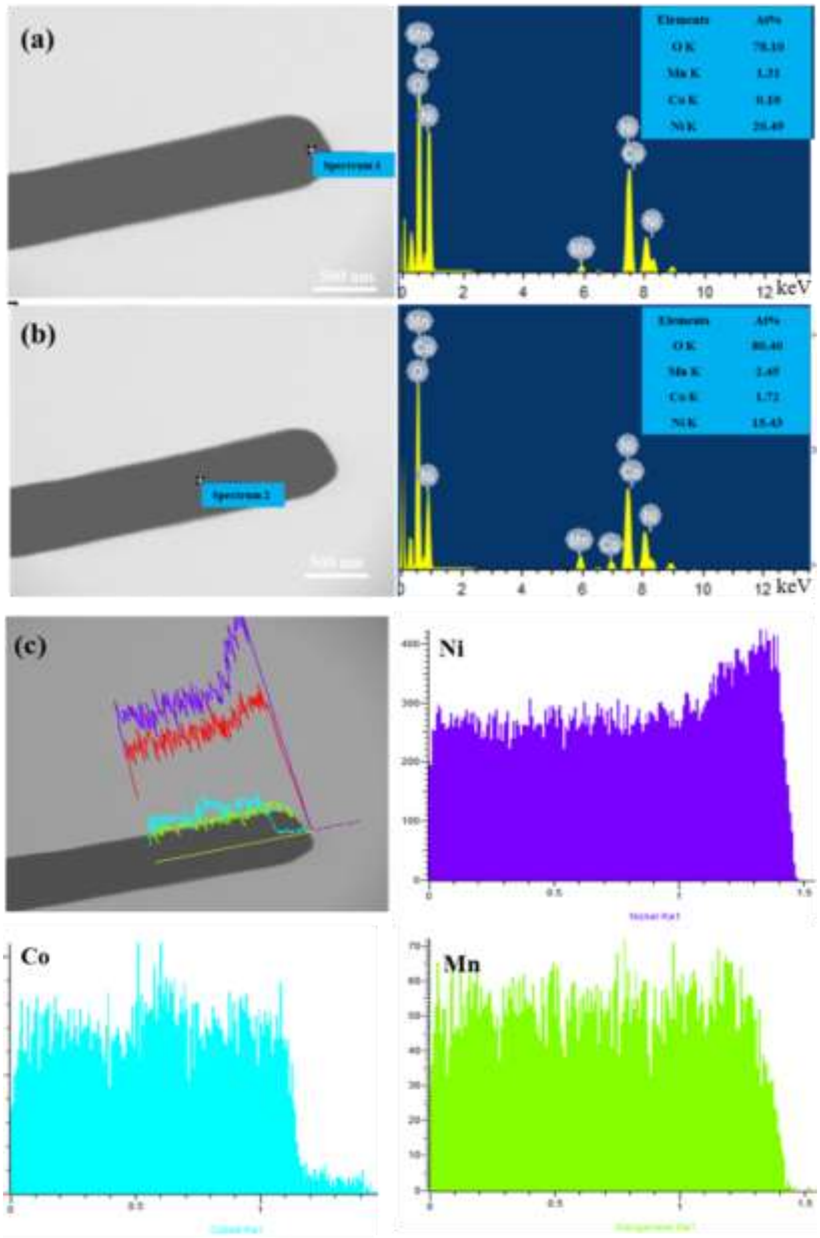

Fig. S7. The EDS spectra of (a) the tip section and (b) the middle section of the $MC_2O_4 \cdot xH_2O$ (M= Ni, Co and Mn) precursor nanorod (for preparation of 1D $LiNi_{0.8}Mn_{0.1}Co_{0.1}O_2$) prepared by sequential precipitation at the second step precipitation of 10 min. (c) EDS elemental line scans for Ni, Co and Mn elements of the nanorod precursor along axial direction.

Fig. S7 shows the EDS spectra and EDS elemental line scans analysis of the $MC_2O_4 \cdot xH_2O$ (M= Ni, Co and Mn) nanorod precursor (for preparation of 1D $LiNi_{0.8}Mn_{0.1}Co_{0.1}O_2$) with the second step precipitation time of 10 min. At the initial stage of the reaction, the precipitate is composed of nanorods with diameters of about 500 nm. The EDS spectra show that the tip section of the nanorod has a low content of cobalt (0.1 wt%), but higher content of nickel (20.49 wt%) and manganese (1.31 wt%), while the middle section has a much higher content of cobalt (1.72 wt%). The EDS results indicate that at the initial stage nickel and manganese attach to the surface of the CoC_2O_4 nanorod and grow into core/shell structure, thus with high content of Co in the center and high content of Ni and Mn in the shell, which is further confirmed by the EDS elemental line scans along the axial direction (Fig. S7c).

Fig. S8

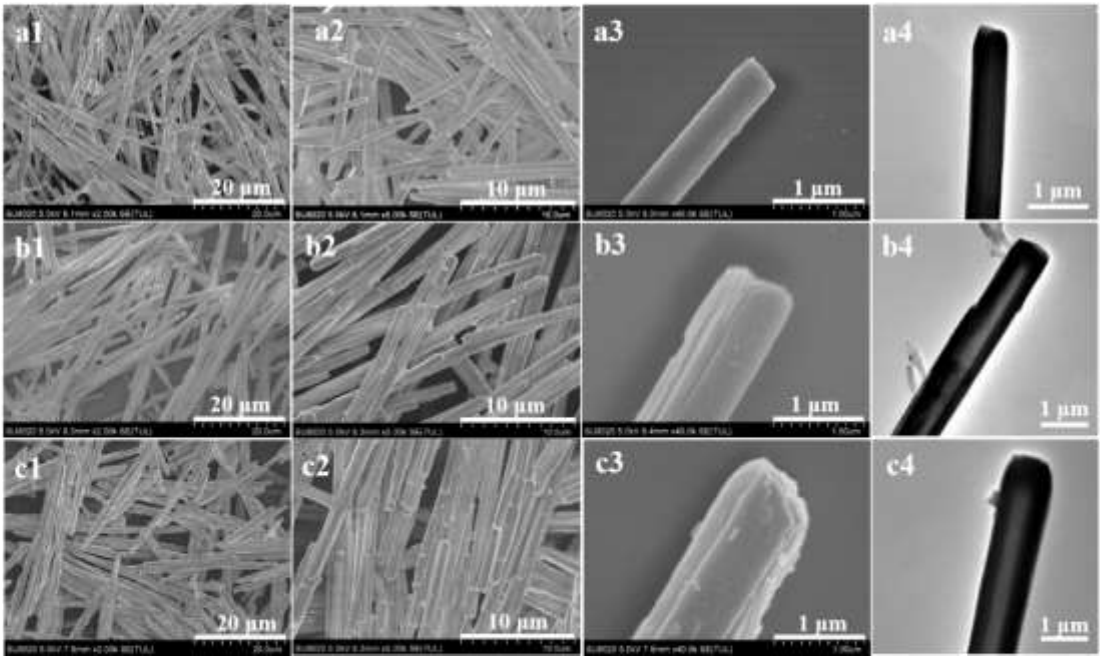

Fig. S8. FESEM and high resolution TEM images of the $MC_2O_4 \cdot xH_2O$ (M= Ni, Co and Mn) precursor for $LiNi_{0.8}Co_{0.1}Mn_{0.1}O_2$ with different reaction time at the second step: (a1–a4) 10 min, (b1-b4) 1 h and (c1-c4) 8 h.

FESEM and TEM images (Fig. S8) show the morphology evolution of the $MC_2O_4 \cdot xH_2O$ (M= Ni, Co and Mn) precursor for $LiNi_{0.8}Mn_{0.1}Co_{0.1}O_2$ with reaction time of 10 min, 1 h and 8 h at the second step, respectively. At the initial stage of the reaction shown in Fig. S8 (a1-a4), the precipitate consists of nanorods with diameters of about 400 nm. As the reaction goes on, the nanorods keep growing and the diameter increases to about 800-850 nm because more $MC_2O_4 \cdot xH_2O$ (M= Mn, Ni) attaches on the nanorod, while $CoC_2O_4 \cdot xH_2O$ diffuses outward as shown in Fig. S8 (b1-b4). When the time increases to 8 h, the oxalate precursor becomes hollow microtubes with diameters of about 1.2 μm as shown in Fig. S8 (c1-c4).

Fig. S9

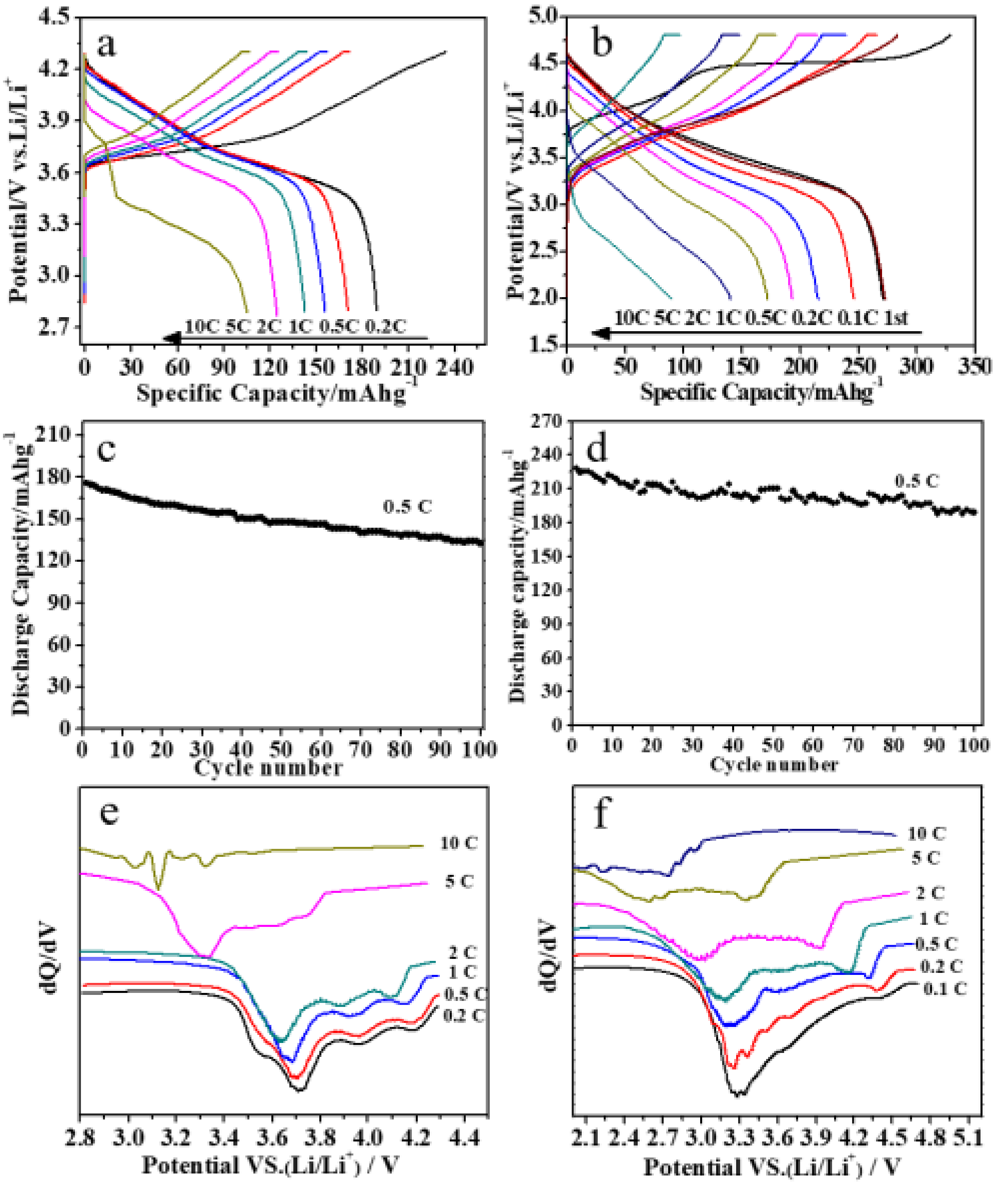

Fig. S9. Electrochemical performances of LNCM-MPs and LR-MPs. (a, b) Charge-discharge profiles of LNCM-MPs and LR-MPs at different rates. (c, d) Cycling performances of LNCM-MPs and LR-MPs at a rate of 0.5 C. (e, f) dQ/dV plots of LNCM811-MPs and LR-MPs at different rates.

Fig. S9a and b show the charge-discharge profiles of LNCM-MPs and LR-MPs at various rates. The initial discharge capacity of the LNCM811-MPs is 188.5 mAh g^{-1} with initial coulombic efficiency of only 79.8% at 0.2 C, and the initial discharge capacity of LR-MPs electrodes is 275.4 mAh g^{-1} with an initial columbic efficiency of 82.6%. The lower initial columbic efficiency and discharge capacity can be ascribed to a smaller surface area and a higher cation disorder of Li^+ and Ni^{2+} related to the two samples.

Fig. S9c and d show the cycling performances of LNCM-MPs and LR-MPs at a rate of 0.5 C, respectively. The corresponding capacity retention ratios are only 75.6% and 76% after 100 cycles. Obviously the samples with microparticle morphology exhibit inferior cycle performance to their microtube counterparts.

Fig. S9e and f show the dQ/dV plots for LNCM-MPs and LR-MPs and the over-potential is obviously higher than those of LNCM811-MTs and LR-MTs, respectively.

Fig. S10

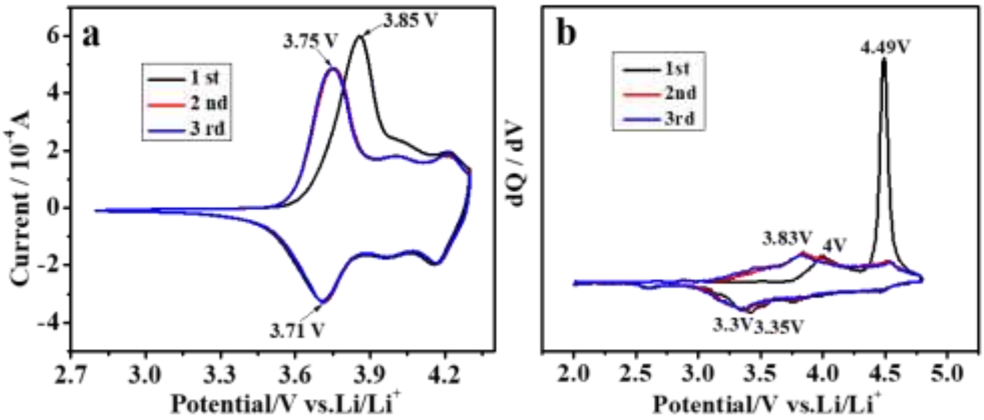

Fig. S10. The first three cycles of (a) the CV curves of the LNCM811-MTs and (b) dQ/dV curves of the LR-MTs at 0.1 C.

Fig. S10a shows the CV curves of LNCM-MTs. LNCM-MTs exhibits an oxidation response at 3.85 V and a corresponding reduction peak at 3.71 V at the first cycle, which corresponds to redox transition of Ni^{3+}/Ni^{4+}, and the potential interval is 0.14 V. The symmetric peaks in following cycles show the excellent reversibility of LNCM811-MTs. Fig. S10b shows the dQ/dV curves of the LR-MTs electrode during the first three cycles. Two oxidation peaks at 4.0 V and 4.49 V can be observed in the first charge process. The first anodic peak at about 4.0 V is predominantly associated with the oxidation of nickel element from Ni^{2+} to Ni^{4+}, and the peak at 4.49 V is mainly associated with the irreversible electrochemical activation reaction which strips Li_2O from the Li_2MnO_3 component to form MnO_2, which is a typical feature of Li-rich cathode materials. The subsequent cycles show peaks associated with the reversible insertion-extraction of lithium ions into the octahedral site of the layered structure centered at 3.83 V upon reduction. The peaks all located at below 3.5 V in discharge progress corresponds to the reduction of Mn^{4+}.

Fig. S11

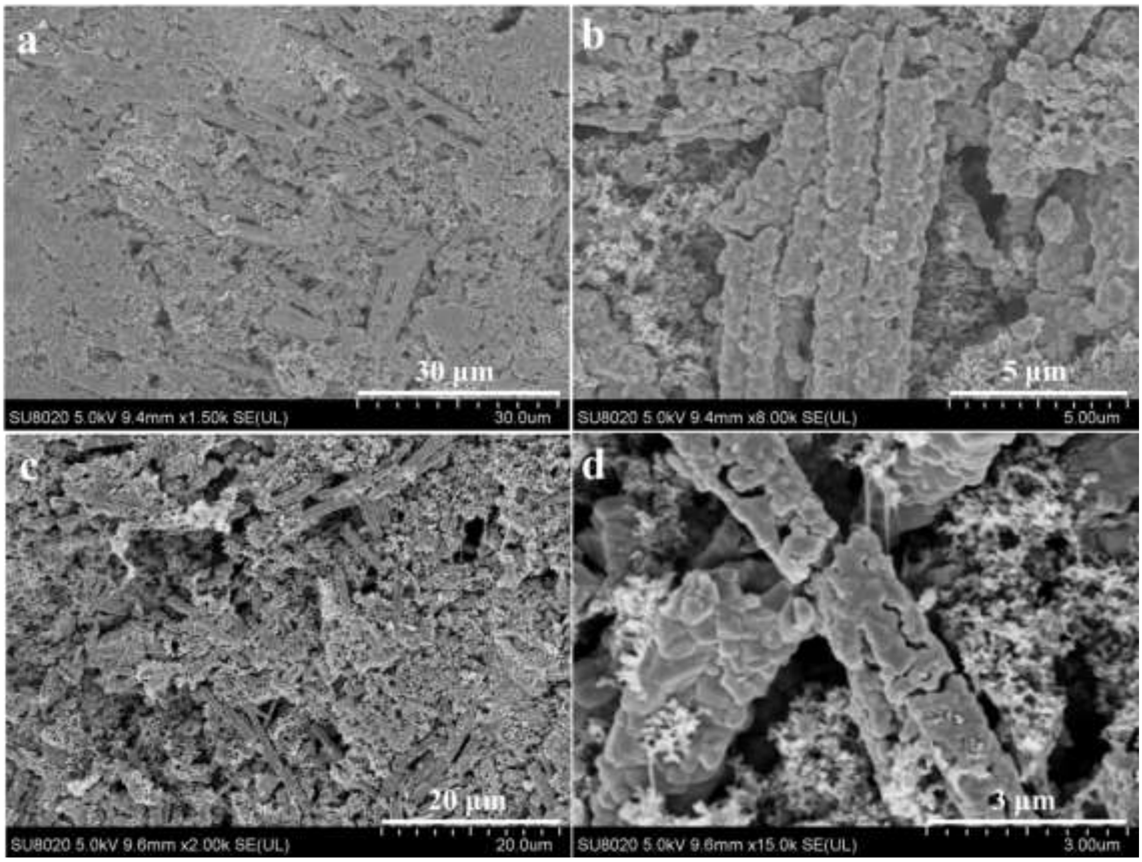

Fig. S11. FESEM images of LNCM811-MTs electrode (a, b) before and (c, d) after 100 charge-discharge cycles at a rate of 0.5 C.

Fig. S12

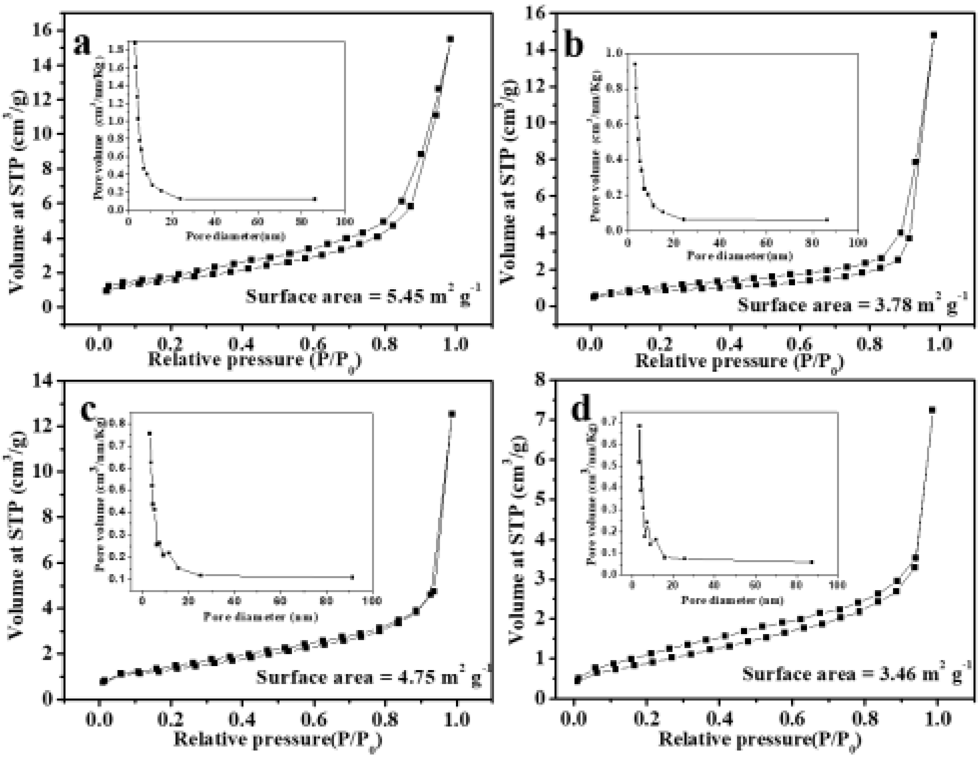

Fig. S12. The N_2 adsorption-desorption isotherms and pore size distribution plots of samples. (a) LNCM811-MTs, (b) LNCM811-MPs; (c) LR-MTs and (d) LR-MPs.

The BET analysis in Fig. S12 shows that the LNCM811-MTs have a higher specific surface area than LNCM811-MPs (5.45 m^2/g versus 3.78 m^2/g) and the LR-MTs have a higher specific surface area than LR-MPs (4.75 m^2/g versus 3.46 m^2/g) due to their morphology and structure differences.

Fig. S13

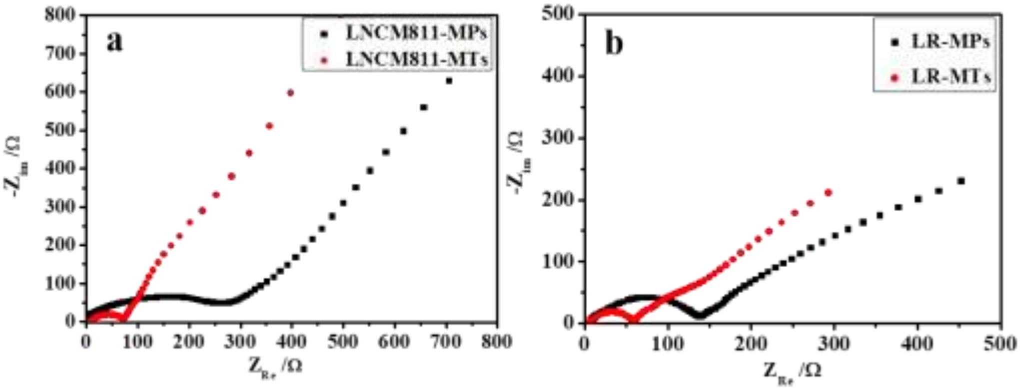

Fig. S13. Nyquist plots of samples. (a) LNCM811-MTs and LNCM811-MPs; (b) LR-MTs and LR-MPs.

The results in Fig. S13 reveal an obvious difference in resistance between microtube and microparticle electrode materials. Generally the diameter of semi-circle at high to medium frequency in the Nyquist plot of the electrode is assigned to the charge-transfer resistance and the inclined line in the low frequency region is attributed to the Warburg diffusion process of the lithium ion into the electrode material (Zw). The charge-transfer resistance of LNCM811-MTs (74.3 Ω) is much lower than that of LNCM811-MPs (272.4 Ω), while that of the LR-MTs (56.3 Ω) is much lower than that of the LR-MPs (135.4 Ω), indicating that 1D hollow structure effectively reduces the barrier for electron and ion transfer at the electrode-electrolyte interface because the unique structure can facilitate shorter diffusion paths for electrons and lithium ions and supply better contact between the active materials and electrolyte.

Fig. S14

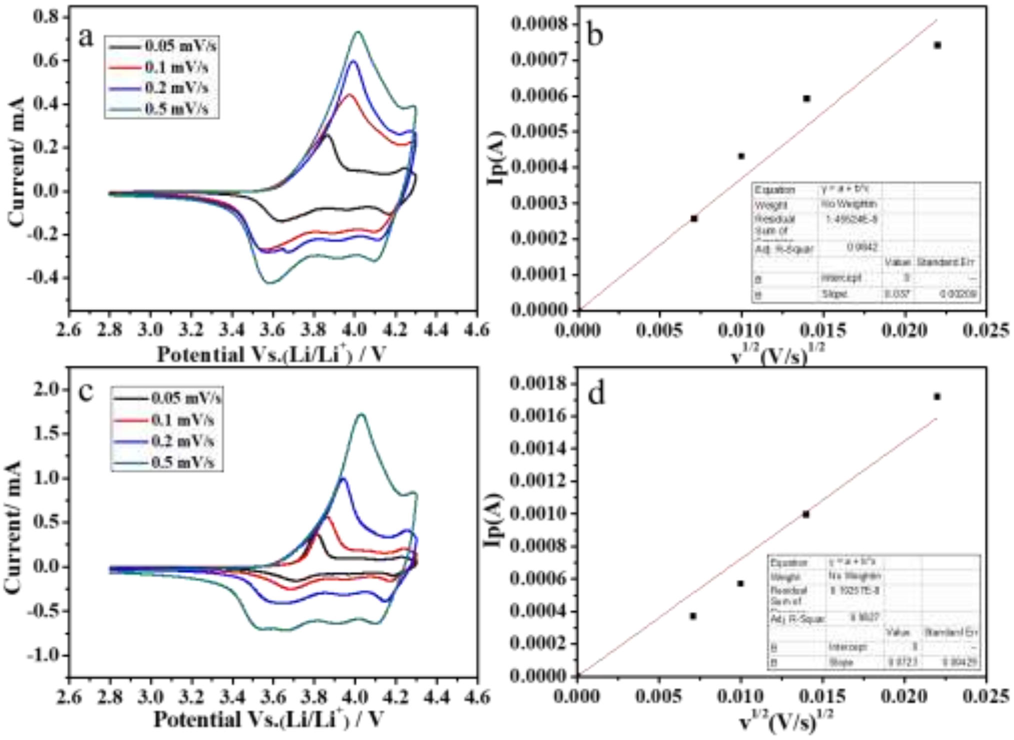

Fig. S14. Cycle voltammograms and peak current *I*p as a function of square root of scan rate $v^{1/2}$ for (a, b) LNCM811-MTs and (c, d) LNCM811-MPs.

The CV peak currents, *I*p, during anodic scans were used to evaluate the Li^+ diffusion coefficient *D*, applying the Randles Sevcik equation[1]:

$$I\mathrm{p}=2.69\times10^{5}\mathrm{n}^{3/2}\mathrm{A}\mathrm{D}^{1/2}v^{1/2}\mathrm{C}$$

where *A* is the electrode area (cm^2), *n* is the number of electrons involved in the redox process (0.8 in our case), *C* is the shuttle concentration (mol cm^{-3}), *v* is the potential scan rate (V s^{-1}), *I*p is in units of amperes, and *D* is in units of cm^2 s^{-1}. Based on the above equation, the Li^+ diffusion coefficients of LNCM811-MTs and LNCM811-MPs were calculated to be 7.86×10^{-7} cm^2 s^{-1} and 3.82×10^{-8} cm^2 s^{-1}, respectively.

Reference in this part:

1. Y. D. Cho, G. T. Fey, H. M. Kao, *J. Power Sources* 2009, **189**, 256–262

Fig. S15

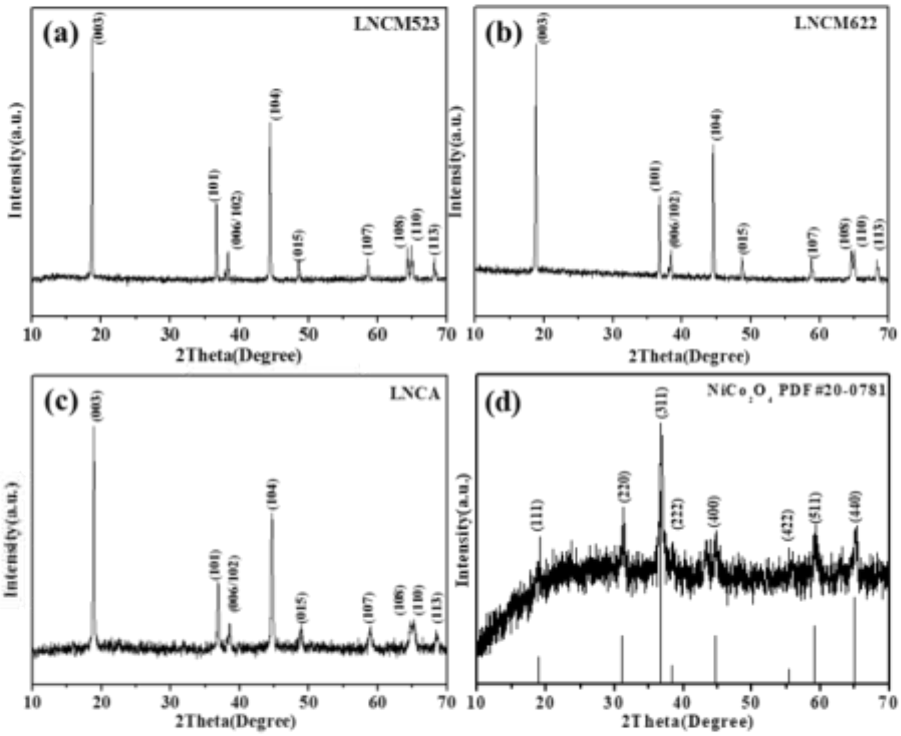

Fig. S15. XRD patterns of (a) $LiNi_{0.5}Co_{0.2}Mn_{0.3}O_2$, (b) $LiNi_{0.6}Co_{0.2}Mn_{0.2}O_2$ and (c) $LiNi_{0.8}Co_{0.15}Al_{0.05}O_2$ microtubes prepared through post-heat treatment of the $MC_2O_4{\cdot}xH_2O$ (M= Ni, Co and Mn) tubular precursor. (d) XRD pattern of $NiCo_2O_4$ nanorod prepared through post-heat treatment of $MC_2O_4{\cdot}xH_2O$ (M= Ni, Co) precursor.

Fig. S15a, b and c show XRD patterns of $LiNi_{0.5}Co_{0.2}Mn_{0.3}O_2$, $LiNi_{0.6}Co_{0.2}Mn_{0.2}O_2$ and $LiNi_{0.8}Co_{0.15}Al_{0.05}O_2$, respectively. All the diffraction peaks of $LiNi_{0.5}Co_{0.2}Mn_{0.3}O_2$, $LiNi_{0.6}Co_{0.2}Mn_{0.2}O_2$ and $LiNi_{0.8}Co_{0.15}Al_{0.05}O_2$ can be indexed to typical α-$NaFeO_2$ layered structure with a space group of $R\bar{3}m$, and no obvious impurity peaks were observed. Fig. S15d shows the XRD pattern of the $NiCo_2O_4$ which can be indexed to the cubic $NiCo_2O_4$ phase (JCPDS card No. 20-0781).

Fig. S16

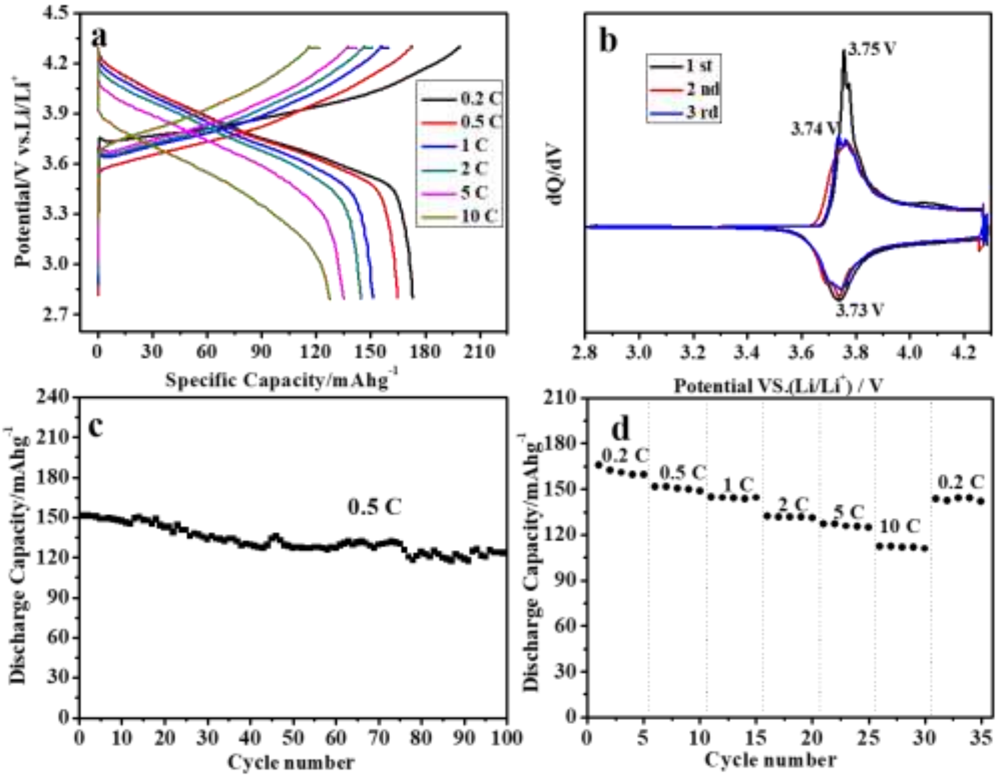

Fig. S16. Electrochemical performances of $LiNi_{0.5}Co_{0.2}Mn_{0.3}O_2$ microtubes. (a) Charge-discharge profiles in the potential range of 2.8 to 4.3 V at various rates. (b) dQ/dV plots at a rate of 0.2 C. (c) Cycling performances at a rate of 0.5 C. (d) Rate capability at different rates.

Electrochemical performances of as-prepared $LiNi_{0.5}Co_{0.2}Mn_{0.3}O_2$ microtube performances are shown in Fig. S16. The as-prepared $LiNi_{0.5}Co_{0.2}Mn_{0.3}O_2$ microtubes deliver discharge capacities of 173.2, 164.7, 151.1, 144.5, 134.9, and 127.5 mAh g^{-1} at the rates of 0.2 C, 0.5 C, 1 C, 2 C, 5 C and 10 C, respectively (Fig. S16a). Their dQ/dV plots (Fig. S16b) exhibit an oxidation response at 3.75 V and a corresponding reduction peak at 3.73 V and their potential interval is 0.02 V, indicating lower polarization during the first cycle and more symmetric peak profile during the following two cycles, which means excellent reversibility of the $LiNi_{0.5}Co_{0.2}Mn_{0.3}O_2$ electrode. Cycling performance at 0.5 C (Fig. S16c) indicates the stable capacity retention at such a high rate. The discharge capacity can maintain a capacity retention of 85.3% at a rate of 0.5 C after 100 cycles. The charge-discharge profiles at different rates from 0.2 C to 10 C at room temperature (Fig. S16d) shows that when the rate returns to 0.2 C, the discharge capacity can return to 153.2 mAh g^{-1}.

Fig. S17

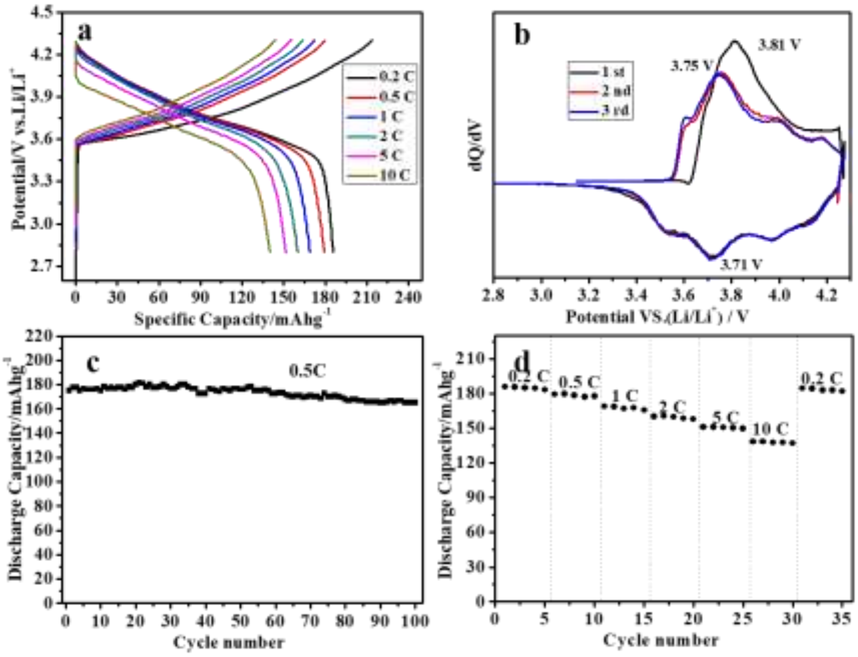

Fig. S17. Electrochemical performances of $LiNi_{0.6}Co_{0.2}Mn_{0.2}O_2$ microtubes. (a) Charge-discharge profiles in the potential range of 2.8 to 4.3 V at various rates. (b) dQ/dV plots at a rate of 0.2 C. (c) Cycling performances at a rate of 0.5 C . (d) Rate capability at different rates.

Electrochemical performances of as-prepared $LiNi_{0.6}Co_{0.2}Mn_{0.2}O_2$ microtubes are shown in Fig. S17. In Fig. S17a, $LiNi_{0.6}Co_{0.2}Mn_{0.2}O_2$ microtubes deliver discharge capacities of 185.6, 179.0, 168.9, 160.1, 151.6 and 139.9 mAh g^{-1} at the rates of 0.2 C, 0.5 C, 1 C, 2 C, 5 C and 10 C, respectively. Their dQ/dV plots display an oxidation response at 3.81 V and a corresponding reduction peak at 3.71 V and their potential interval is 0.1 V (Fig. S17b), indicating low polarization during the first cycle and symmetric peak profile during the following two cycles, which means good reversibility of the $LiNi_{0.6}Co_{0.2}Mn_{0.2}O_2$. Cycling performance at 0.5 C (Fig. S17c) shows the stable capacity retention. The discharge capacity can maintain a capacity retention of 94.2% at 0.5 C after 100 cycles. The charge-discharge profiles at different rates from 0.2 C to 10 C at room temperature (Fig. S17d) indicate that when the rate returns to 0.2 C, the discharge capacity can come back to 186.4 mAh g^{-1}.

Fig. S18

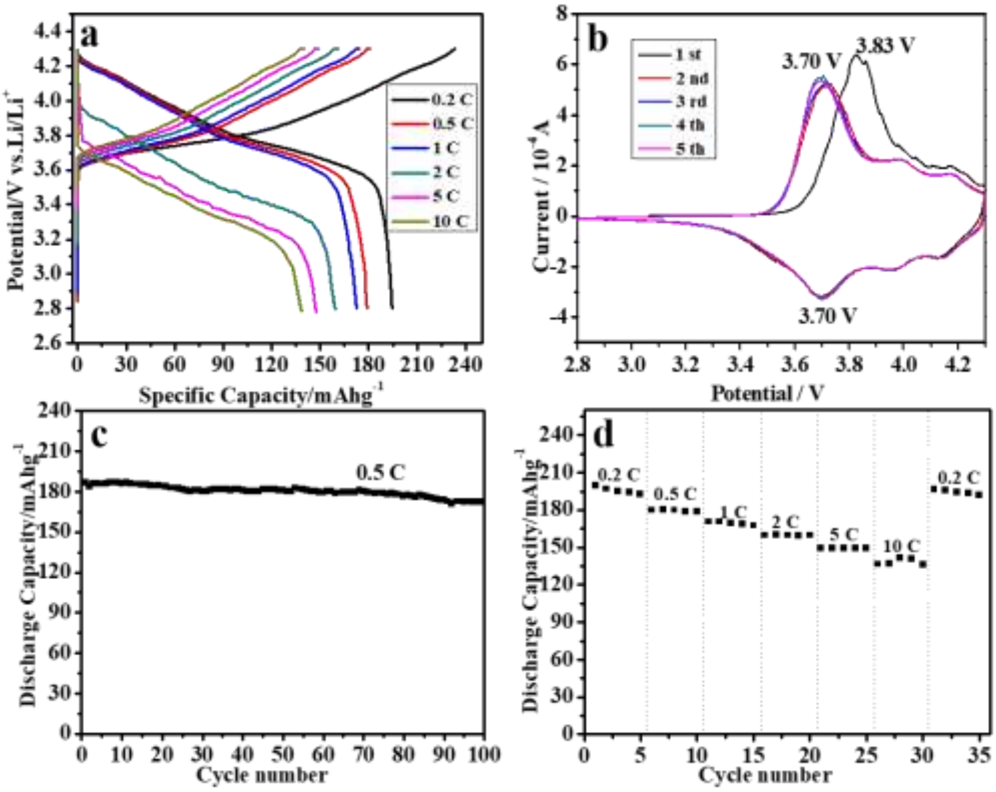

Fig. S18. Electrochemical performances of $LiNi_{0.8}Co_{0.15}Al_{0.05}O_2$ microtubes. (a) Charge-discharge profiles in the potential range of 2.8 to 4.3 V at various rates. (b) Cyclic voltammetry curves between 2.8 V and 4.3 V at a scan rate of 0.1mV·s^{-1}. (c) Cycling performances at a rate of 0.5 C. (d) Rate capability at different rates.

Electrochemical performances of as-prepared $LiNi_{0.8}Co_{0.15}Al_{0.05}O_2$ microtubes are shown in Fig. S18. In Fig. S18a, $LiNi_{0.8}Co_{0.15}Al_{0.05}O_2$ microtubes deliver discharge capacities of 194.5, 179.3, 172.5, 159.5, 147.6 and 138.6 mAh g^{-1} at the rates of 0.2 C, 0.5 C, 1 C, 2 C, 5 C and 10 C, respectively. The dQ/dV plots display an oxidation response at 3.83 V and a corresponding reduction peak at 3.70 V and their potential interval is 0.13 V (Fig. S18b), indicating low polarization during the first cycle and symmetric peak profile during the following two cycles, which means good reversibility of the $LiNi_{0.8}Co_{0.15}Al_{0.05}O_2$. Cycling performances at a rate of 0.5 C (Fig. S18c) indicate the stable capacity retention. The discharge capacity can maintain a capacity retention of 91.8% at a rate of 0.5 C after 100 cycles. The charge-discharge profiles at different rates from 0.2 C to 10 C at room temperature (Fig. S18d) show that when the rate returns to 0.2 C, the discharge capacity can still reach 194.3 mAh g^{-1}.

Fig. S19

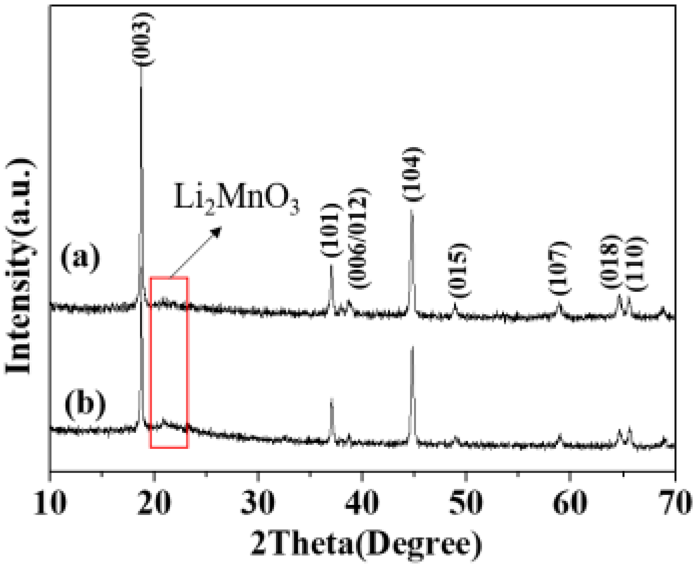

Fig. S19 XRD patterns of the as-prepared doped Li-rich samples. (a) $Li_{1.2}Ni_{0.13}Co_{0.10}Mn_{0.54}Fe_{0.03}O_2$ and (b) $Li_{1.2}Ni_{0.10}Co_{0.13}Mn_{0.54}Cu_{0.03}O_2$ products.

The XRD patterns of Fe and Cu doped Li-Rich samples are shown in Fig. S19. All diffraction peaks can be indexed to hexagonal a-$NaFeO_2$ structure without obvious impurity phase. The main diffraction peaks could be indexed to $R\bar{3}m$ space group, which belongs to the layered $LiMO_2$ (M = Ni, Co, Mn). The weak superlattice peaks, between 20° and 25°, can be attributed to monoclinic Li_2MnO_3 component with C2/m space group. The Fe and Cu doped Li-Rich samples show no differences in XRD patterns from the bare one, indicating that small amount of the doping elements has no obvious impact on the structure [1].

Reference in this part:

1 Y. H. Xiang, J. Li, X. W. Wu, Z. X. Liu, Z. Q. He and Z. L. Yin. *Ceram. Int.* 2016, **42**: 8833-8838.

Fig. S20

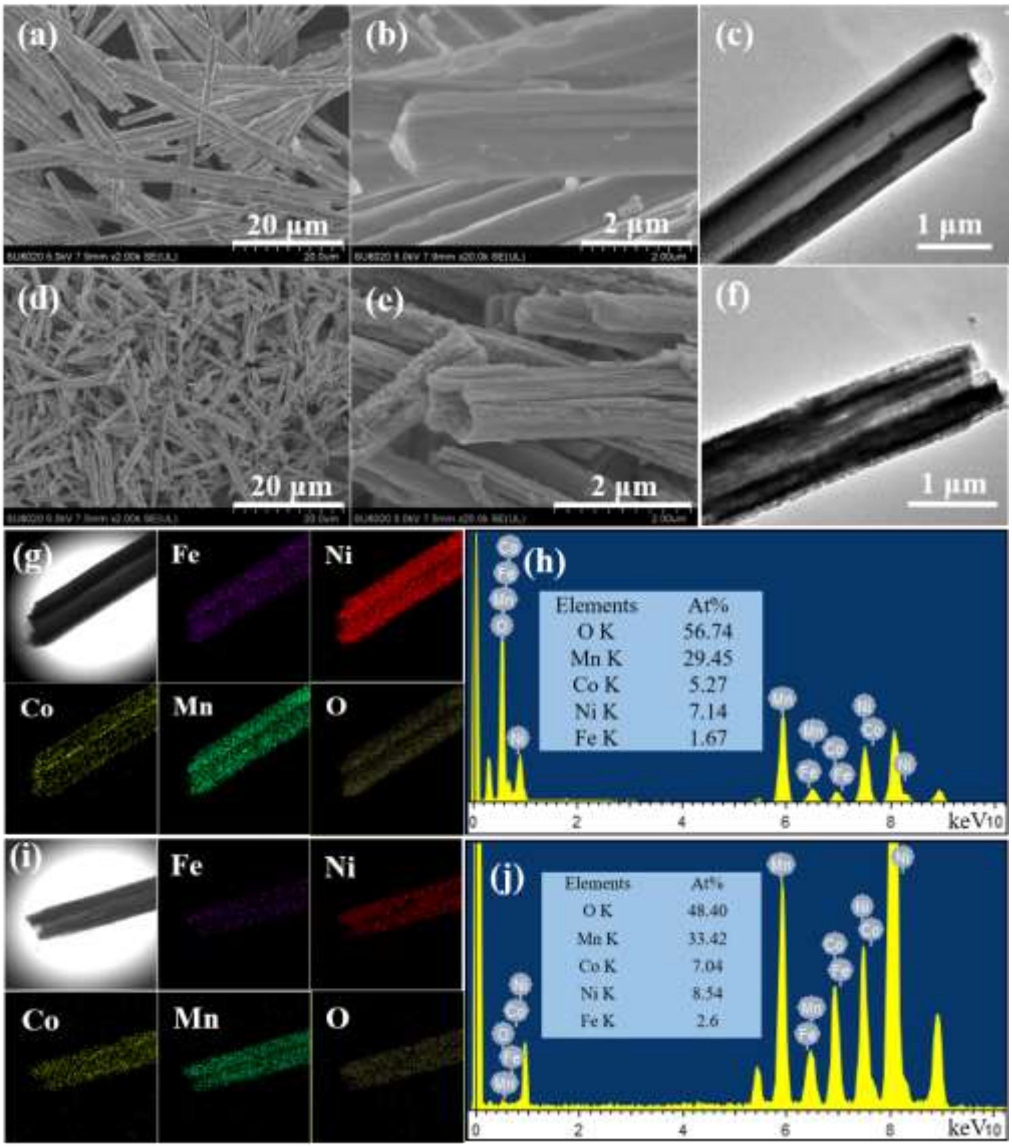

Fig. S20 (a, b) FESEM and (c) TEM images of $MC_2O_4{\cdot}xH_2O$ (M= Ni, Co, Mn and Fe) precursor for $Li_{1.2}Ni_{0.13}Co_{0.10}Mn_{0.54}Fe_{0.03}O_2$. (d, e) FESEM and (f) TEM images of $Li_{1.2}Ni_{0.13}Co_{0.10}Mn_{0.54}Fe_{0.03}O_2$ product. (g) EDS elemental mappings (Ni, Co, Mn, Fe and O) and (h) EDS spectrum of $MC_2O_4{\cdot}xH_2O$ (M= Ni, Co, Mn and Fe) precursor for $Li_{1.2}Ni_{0.13}Co_{0.10}Mn_{0.54}Fe_{0.03}O_2$ microtube. (i) EDS elemental mappings (Ni, Co, Mn, Fe and O) and (j) EDS spectrum of $Li_{1.2}Ni_{0.13}Co_{0.10}Mn_{0.54}Fe_{0.03}O_2$ microtube.

FESEM and TEM images in Fig. S20 show that the metal oxalate precursor and $Li_{1.2}Ni_{0.13}Co_{0.10}Mn_{0.54}Fe_{0.03}O_2$ product are composed of large scale of microrods. Fig. S20a and b show that the metal oxalate precursor microrods display diameters of 1-2 μm and lengths of 20-60 μm, and the hollow structure is demonstrated by the TEM image in Fig. S20c. Fig. S20d and e show that the $Li_{1.2}Ni_{0.13}Co_{0.10}Mn_{0.54}Fe_{0.03}O_2$ microrods exhibit diameters of about 1 μm and lengths of 10-20 μm. In Fig. S20e, the hollow structure of the $Li_{1.2}Ni_{0.13}Co_{0.10}Mn_{0.54}Fe_{0.03}O_2$ can be obviously observed, which is further confirmed by the TEM image (Fig. S20f). The diameter and length of $Li_{1.2}Ni_{0.13}Co_{0.10}Mn_{0.54}Fe_{0.03}O_2$ product is smaller than that of the metal oxalate precursor due to the shrinkage and breaking of the samples during the calcination process.

The elemental mappings of $MC_2O_4 \cdot xH_2O$ (M= Ni, Co, Mn, Fe and O) precursor for $Li_{1.2}Ni_{0.13}Co_{0.10}Mn_{0.54}Fe_{0.03}O_2$ in Fig. S20g show uniform distribution of Ni, Co, Mn, Fe and O elements along the axial direction with hollow interior. The atomic ratio of Ni, Co, Mn and Fe (Fig S20h) is 1:0.74:4.12:0.23, which is close to that of the $MC_2O_4 \cdot xH_2O$ (M= Ni, Co, Mn, Fe and O) precursor (比例多少？). The results in Fig. S20i show uniform distribution of Ni, Co, Mn, Fe and O elements in the $Li_{1.2}Ni_{0.13}Co_{0.10}Mn_{0.54}Fe_{0.03}O_2$ along the axial direction with hollow interior, which is consistent with the precursor shown in Fig. S20g. The element ratio of Ni, Co, Mn and Fe is about 1:0.82:3.91:0.23 in Fig. S20j, which is close to the theoretical ratio of the $Li_{1.2}Ni_{0.13}Co_{0.10}Mn_{0.54}Fe_{0.03}O_2$ product (Ni:Co:Mn:Fe=1:0.77:4:0.23).

Fig. S21

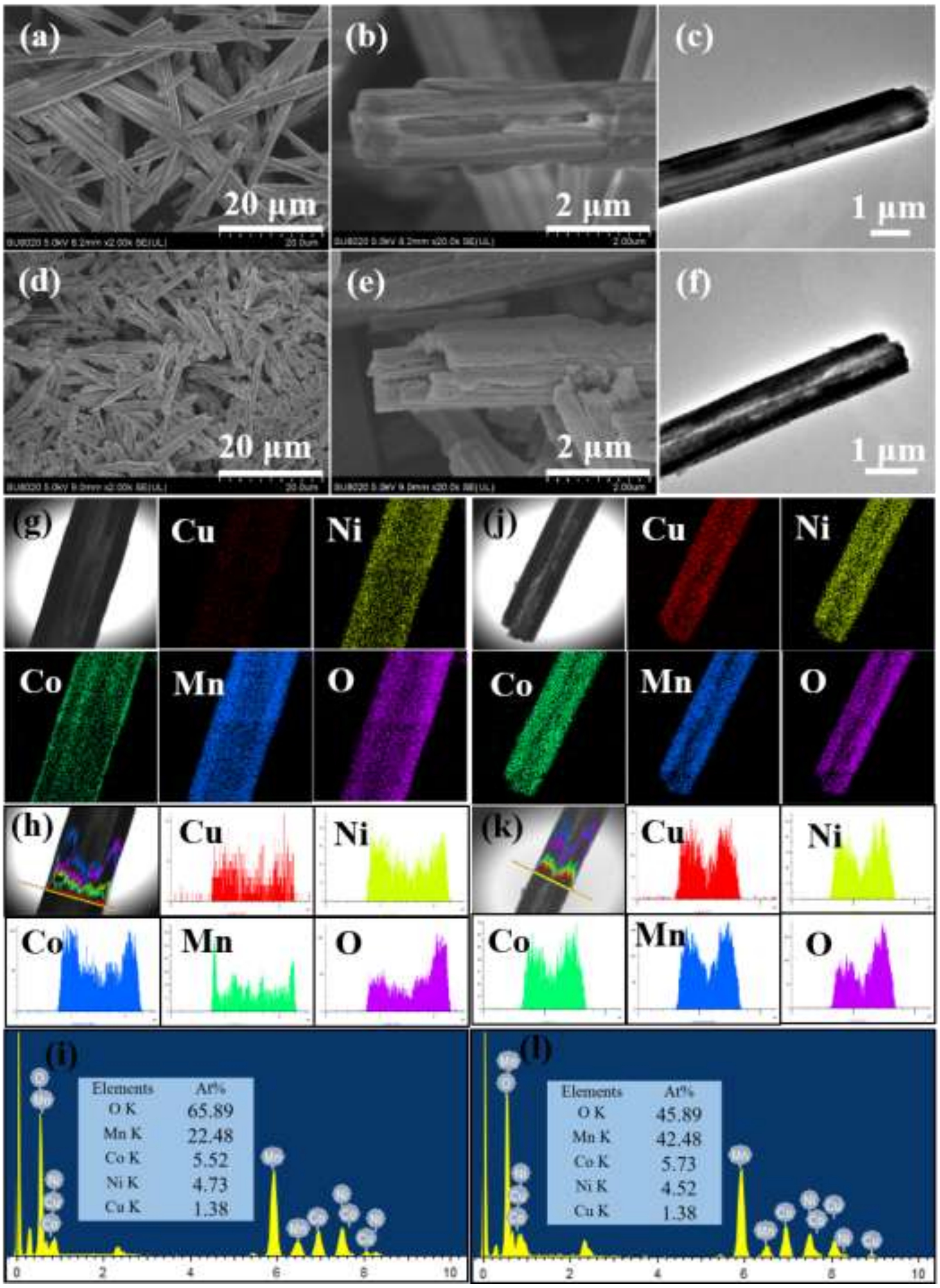

Fig. S21 (a, b) FESEM and (c) TEM images of $MC_2O_4 \cdot xH_2O$ (M= Ni, Co, Mn and Cu) precursor for $Li_{1.2}Ni_{0.10}Co_{0.13}Mn_{0.54}Cu_{0.03}O_2$ and (d, e) FESEM and (f) TEM images of $Li_{1.2}Ni_{0.10}Co_{0.13}Mn_{0.54}Cu_{0.03}O_2$ product. (g) EDS elemental mappings, (h) line scans (Ni, Co, Mn, Cu and O) and (i) EDS spectrum of

$MC_2O_4 \cdot xH_2O$ (M=Ni, Co, Mn and Cu) precursor for $Li_{1.2}Ni_{0.10}Co_{0.13}Mn_{0.54}Cu_{0.03}O_2$. (j) EDS elemental mapping, (k) line scans (Ni, Co, Mn, Cu and O) and (l) EDS spectrum of $Li_{1.2}Ni_{0.10}Co_{0.13}Mn_{0.54}Cu_{0.03}O_2$ product.

FESEM and TEM images in Fig. S21 show the metal oxalate precursor and $Li_{1.2}Ni_{0.10}Co_{0.13}Mn_{0.54}Cu_{0.03}O_2$ product are composed of large scale of microrods. Fig. S21a and b show that the metal oxalate precursor microrods display diameters of 1-2 μm and lengths of 20-60 μm, and the hollow structure is demonstrated by the TEM image in Fig. S21c. Fig. S21d and e show that the $Li_{1.2}Ni_{0.10}Co_{0.13}Mn_{0.54}Fe_{0.03}O_2$ microrods exhibit diameters of about 1 μm and lengths of 10-20 μm. In Fig. S21e, the hollow structure of the $Li_{1.2}Ni_{0.10}Co_{0.13}Mn_{0.54}Cu_{0.03}O_2$ can be obviously observed, which is further confirmed by the TEM image (Fig. S21f). The diameter and length of $Li_{1.2}Ni_{0.10}Co_{0.13}Mn_{0.54}Cu_{0.03}O_2$ product is smaller than that of the metal oxalate precursor for the shrinkage and breaking of the samples during the calcination process.

The elemental mappings of $MC_2O_4 \cdot xH_2O$ (M= Ni, Co, Mn, Cu and O) precursor for $Li_{1.2}Ni_{0.10}Co_{0.13}Mn_{0.54}Cu_{0.03}O_2$ (Fig. S21g) show uniform distribution of Ni, Co, Mn, Fe and O elements along the axial direction with hollow interior, which is further confirmed by EDS elemental line scans along the radial direction (Fig. S21h). The atomic ratio of Ni, Co, Mn and Cu is 0.86:1:4.07:0.25, which is close to that of $MC_2O_4 \cdot xH_2O$ (M= Ni, Co, Mn and Cu) precursor (Ni:Co:Mn:Cu=0.77:1:4:0.23) (Fig. S21i).

The results in Fig. S21j show uniform distribution of Ni, Co, Mn, Cu and O elements in the $Li_{1.2}Ni_{0.10}Co_{0.13}Mn_{0.54}Cu_{0.03}O_2$ along the axial direction with hollow interior, which is further confirmed by the line scans in Fig. S21k. The atomic ratio of Ni, Co, Mn and Cu is about 0.76:1:3.66:0.23 (Fig. S21l), which is close to the theoretical ratio of the $Li_{1.2}Ni_{0.10}Co_{0.13}Mn_{0.54}Cu_{0.03}O_2$ product (Ni:Co:Mn:Cu=0.77:1:4:0.23).

Fig. S22

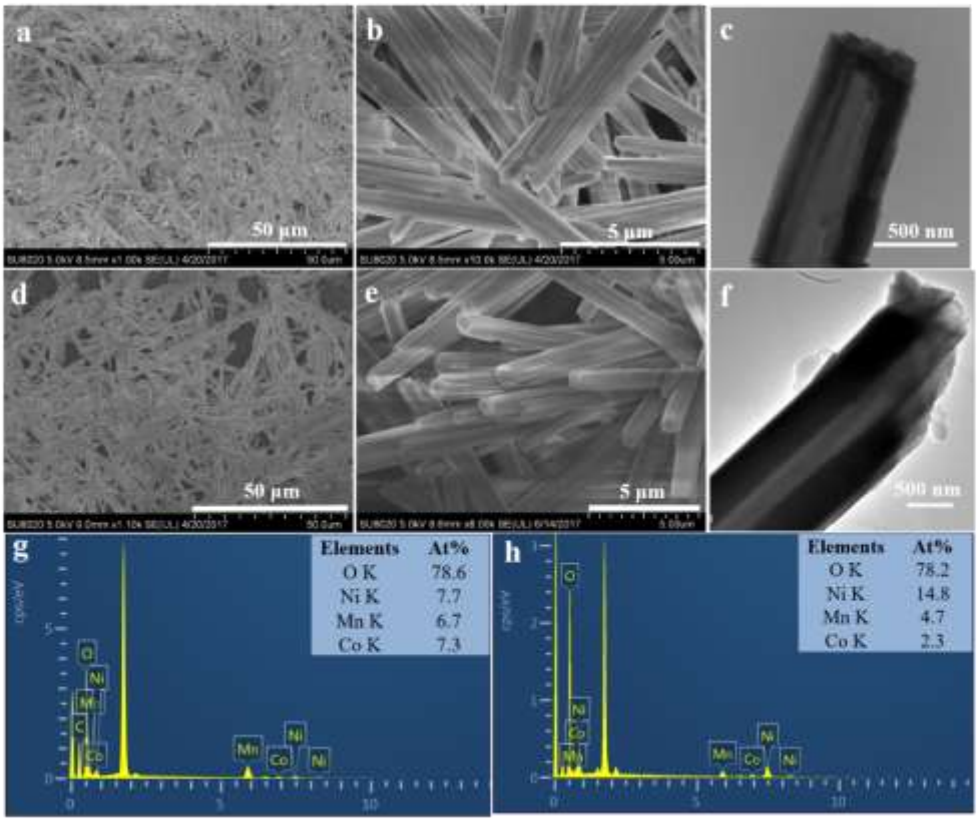

g

Elements	At%
O K	78.6
Ni K	7.7
Mn K	6.7
Co K	7.3

h

Elements	At%
O K	78.2
Ni K	14.8
Mn K	4.7
Co K	2.3

Fig. S22. FESEM images of $MC_2O_4 \cdot xH_2O$ (M= Ni, Co and Mn) precursors for (a, b) $LiNi_{1/3}Co_{1/3}Mn_{1/3}O_2$ and (d, e) $LiNi_{0.7}Co_{0.1}Mn_{0.2}O_2$. High resolution TEM images of $MC_2O_4 \cdot xH_2O$ (M= Ni, Co and Mn) for (c) $LiNi_{1/3}Co_{1/3}Mn_{1/3}O_2$ and (f) $LiNi_{0.7}Co_{0.1}Mn_{0.2}O_2$. EDS spectra of (g) $LiNi_{1/3}Co_{1/3}Mn_{1/3}O_2$ and (h) $LiNi_{0.7}Co_{0.1}Mn_{0.2}O_2$.

FESEM images in Fig. S22a, b, d and e show the uniform microrod morphology of $MC_2O_4 \cdot xH_2O$ (M= Ni, Co and Mn) precursor for $LiNi_{1/3}Co_{1/3}Mn_{1/3}O_2$ and $LiNi_{0.7}Co_{0.1}Mn_{0.2}O_2$. The hollow structure is confirmed by the high resolution TEM images in Fig. S22c and f. The atomic ratio of the Ni, Co and Mn of $MC_2O_4 \cdot xH_2O$ precursor in Fig. S22g and h are 1.15:1.09:1 and 6.43:1:2.04 which are in agreement with the composition of the $LiNi_{1/3}Co_{1/3}Mn_{1/3}O_2$ and $LiNi_{0.7}Co_{0.1}Mn_{0.2}O_2$, respectively.

Fig. S23

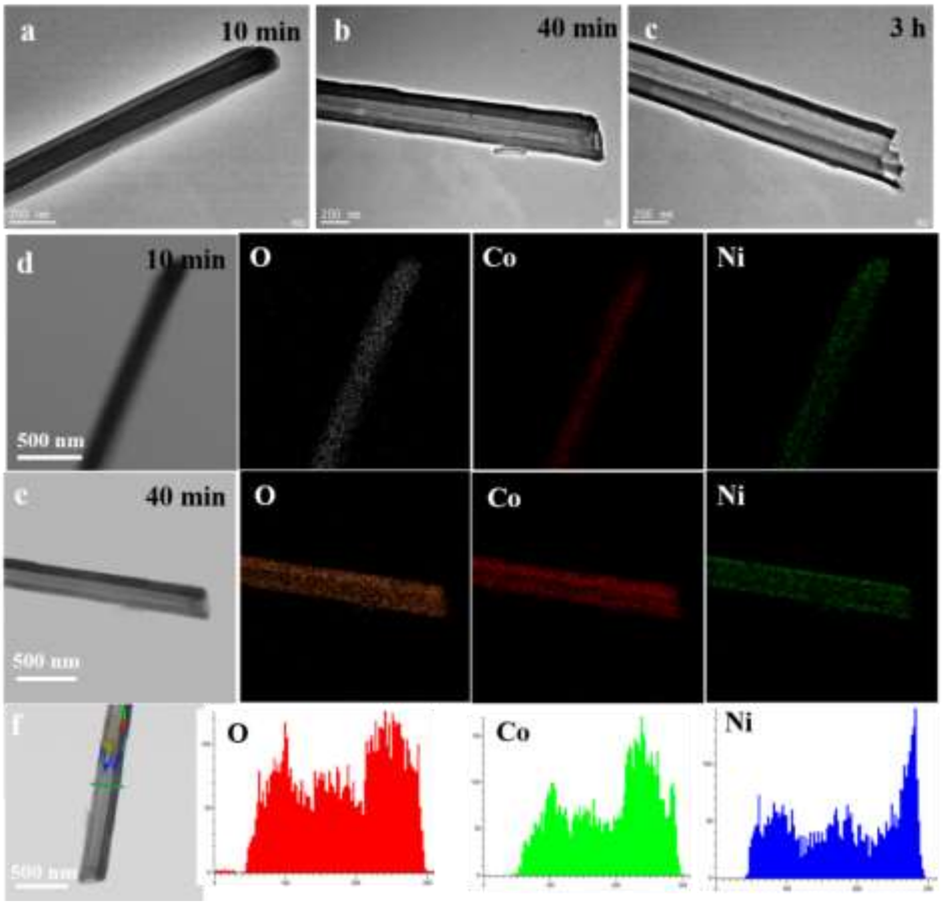

Fig. S23. High resolution TEM images of the oxalate precursor for $NiCo_2O_4$ with reaction time of (a) 10 min, (b) 40 min and (c) 3 h at the second precipitation step. EDS elemental mapping images of the oxalate precursor with reaction time of (d) 10 min and (e) 40 min at the second precipitation step. (f) EDS elemental line scans of the oxalate precursor along the axial direction with reaction time of 40 min at the second precipitation step.

Fig. S23a, b and c show the TEM image evolution of the $MC_2O_4 \cdot xH_2O$ (M= Ni, Co and Mn,) precursor for $NiCo_2O_4$ with the reaction time of 10 min, 40 min and 3 h at the second precipitation step, respectively. At the initial stage of the reaction, the morphology of the precipitates is core/shell structure nanorod with diameters of about 200 nm. As the reaction going on, the nanorod grows hollow for the non-equilibrium interdiffusion and the hollow space increasing in size. When the time comes to 3 h, the morphology of the oxalate precursor becomes hollow. The EDS elemental mapping of the Ni, Co and O in Fig. S23d and e further confirm the evolution from core/shell structure to hollow structure of the oxalate precursor. The hollow structure is further confirmed by EDS elemental line scan along the axial direction (Fig. S23f).

Fig. S24

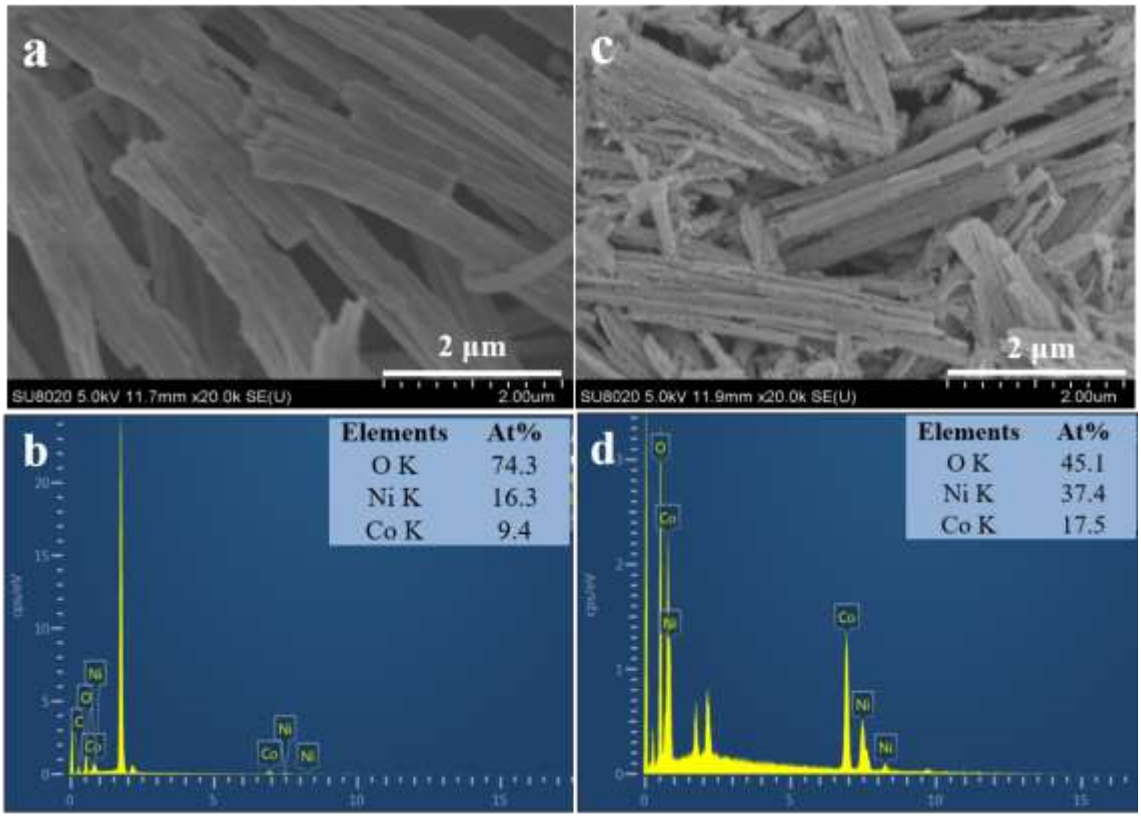

Fig. S24. FESEM images and EDS spectra of (a, b) $MC_2O_4 \cdot xH_2O$ (M= Ni, Co) nanotubes for preparation of (c, d) $NiCo_2O_4$ anode materials.

FESEM images in Fig. S24a shows the nanotube morphology of the $MC_2O_4 \cdot xH_2O$ (M= Ni, Co). Fig. S24c shows porous nanotube morphology of $NiCo_2O_4$ and the porous structure is generated by the release of gas during the decomposition process of the oxalate precursor. The atomic ratios of Ni and Co of $MC_2O_4 \cdot xH_2O$ precursor and $NiCo_2O_4$ product (Fig. S24b and d) are both close to 1:2 which is in good agreement with that of $NiCo_2O_4$.

Fig. S25

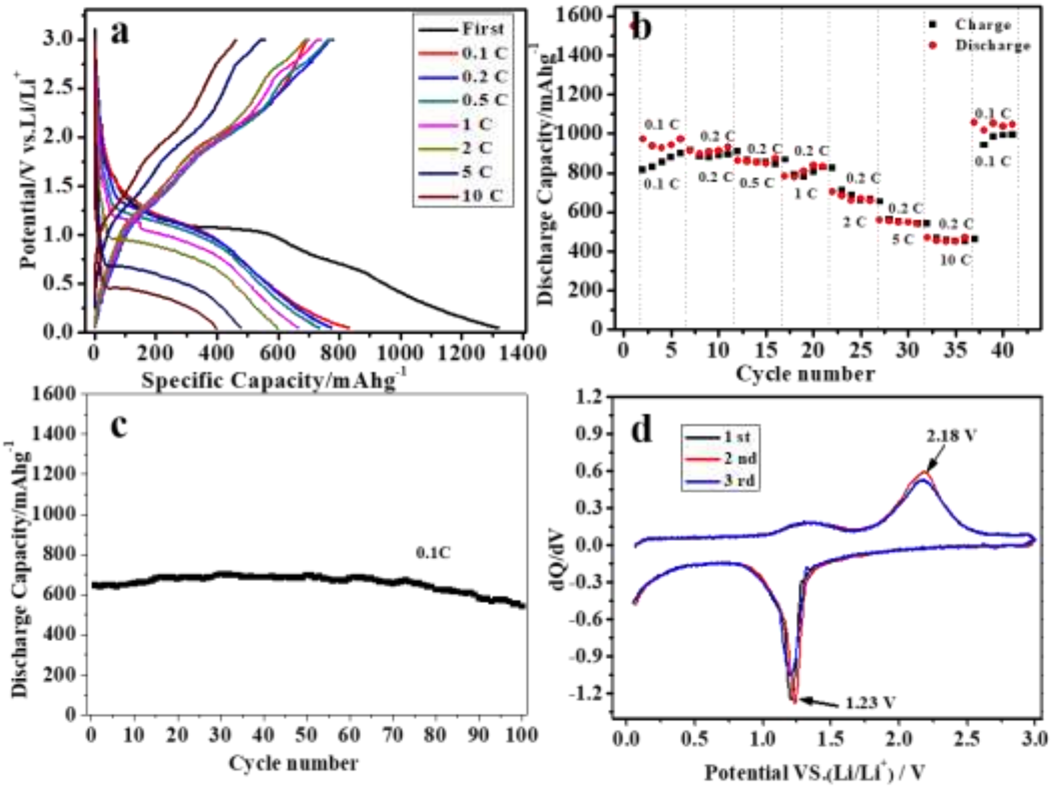

Fig. S25. Electrochemical performances of $NiCo_2O_4$ nanotube as LIB anode material. (a) Charge-discharge profiles in the potential range of 0.05 to 3 V at various rates. (b) Rate capability at different rates.(c) Cycling performances at a rate of 1 C. (d) dQ/dV plots at a rate of 0.1 C.

The $NiCo_2O_4$ nanotubes (Fig. S25a) deliver discharge capacities of 1316.1 mAh g^{-1} at the first cycle and 829.7, 775.1, 729.5, 659.6, 595.7, 447.2 and 398.2 mAh g^{-1} at the rates of 0.1 C, 0.2 C, 0.5 C, 1 C, 2 C, 5 C and 10 C, respectively. When the rate returns to 0.1 C, the discharge capacity can still match the initial capacity (Fig. S25b). Cycling performances of the $NiCo_2O_4$ nanotubes at a rate of 1 C (Fig. S25c) indicate its excellent cycling stability. The discharge capacity can maintain a capacity retention of 84.6% at a rate of 1 C after 100 cycles. dQ/dV plots (Fig. S29d) at a rate of 0.1 C exhibit an oxidation response at 2.18 V and a corresponding reduction peak at 1.23 V and more symmetric peak profile during the following two cycles, which means excellent reversibility of the $NiCo_2O_4$ electrode.

Fig. S26

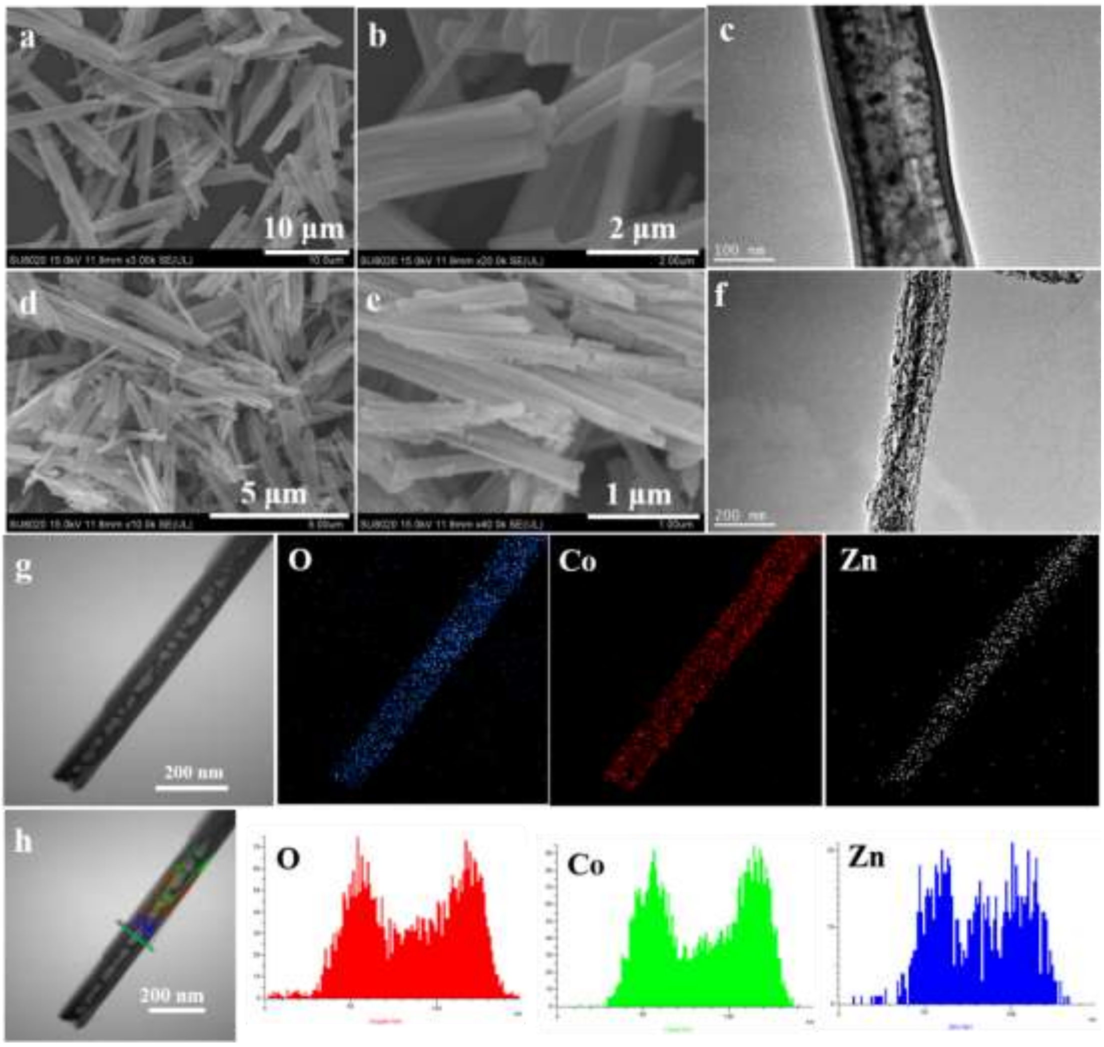

Fig. S26. FESEM images of (a, b) $MC_2O_4{\cdot}xH_2O$ (M= Zn, Co) precipitates as precursors for preparation of (d, e) $ZnCo_2O_4$ anode materials. TEM images of (c) $MC_2O_4{\cdot}xH_2O$ (M= Zn, Co) precursors and (f) $ZnCo_2O_4$ anode materials. (g) EDS elemental mapping of O, Co, Zn and (h) EDS line scans along the radial direction of $MC_2O_4{\cdot}xH_2O$ (M= Zn, Co) precursor.

Fig. S26 shows (a, b) FESEM and (c) TEM images of $MC_2O_4{\cdot}xH_2O$ (M= Zn, Co) precipitates as precursors for preparation of $ZnCo_2O_4$ as anode materials with reaction time of 3 h at the second step. The precipitate is composed of nanotubes with diameters of about 150 nm. FESEM and TEM images of $ZnCo_2O_4$ (Fig. S26d, e and f) show that the nanotube morphology is retained after calcining in the air and porous structure is generated for the release of gas during the decomposition process of the oxalate precursor. The hollow structure and elements distribution of the nanotube precursors are further confirmed by EDS elemental mapping and line scans of the Ni, Co and O elements along the radial direction in Fig. S26g, h.

Fig. S27

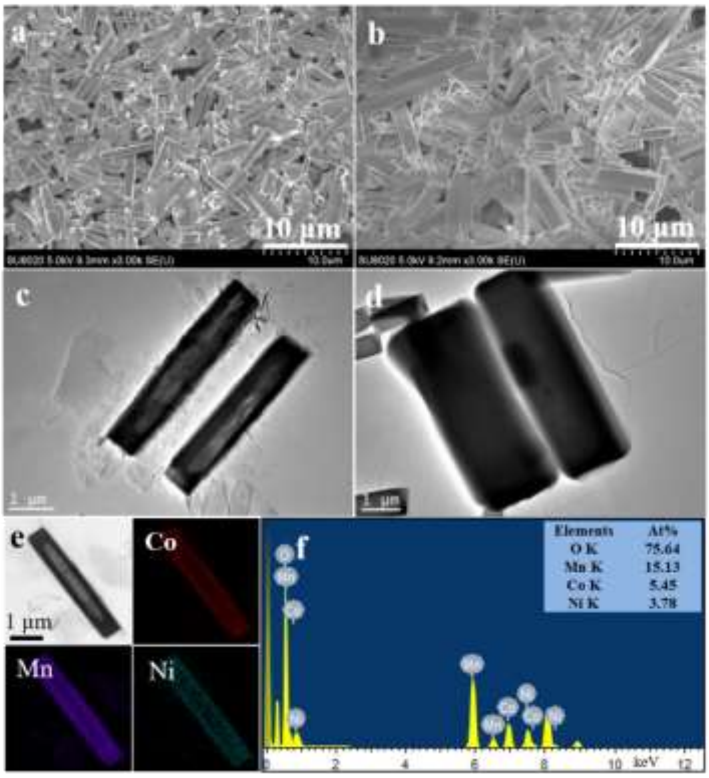

Fig. S27. FESEM images and high resolution TEM images of $MC_2O_4{\cdot}xH_2O$ (M= Ni, Co and Mn) precursor for Li-rich $0.5Li_2MnO_3{\cdot}0.5LiNi_{1/3}Co_{1/3}Mn_{1/3}O_2$ via (a, c) sequential precipitation or (b, d) co-precipitation. (e) EDS elemental mapping and (f) spectrum of $MC_2O_4{\cdot}XH_2O$ (M= Ni, Co and Mn) precursor via sequential precipitation.

FESEM images (Fig. S27a and b) show that the as-prepared $MC_2O_4{\cdot}xH_2O$ (M= Ni, Co and Mn) precursors via different synthetic routes are composed of large scale of microrods. However, the obviously hollow microtube as the precursor synthesized via sequential precipitation is confirmed by TEM image (Fig. S27c), while the precursor synthesized via co-precipitation is solid microrod (Fig. S27d). The microtube morphology and elements distribution of the precursor prepared via sequential precipitation is further confirmed by EDS elemental mapping (Fig. S27e). The atom ratio of Ni, Co and Mn in Fig. S27f is 1:1.4:4 which is close to that of the $0.5Li_2MnO_3{\cdot}0.5LiNi_{1/3}Co_{1/3}Mn_{1/3}O_2$ (Ni:Co:Mn=1:1:4).

Fig. S28

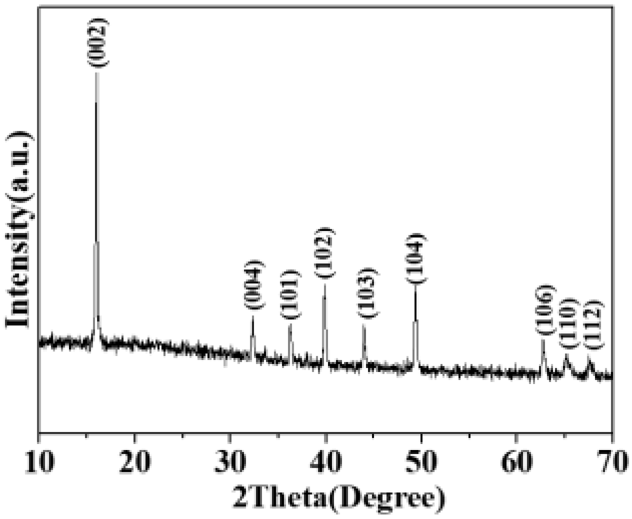

Fig. S28 XRD pattern of $Na_{0.56}Ni_{0.13}Co_{0.13}Mn_{0.54}O_2$ product.

XRD analysis was conducted to further confirm the composition of as-prepared product as shown in Fig. S28. All the diffraction peaks of $Na_{0.56}Ni_{0.13}Co_{0.13}Mn_{0.54}O_2$ product can be indexed to a typical P2-type structure with a $P6_3/mmc$ space group, in which Co, Mn and Ni are located in octahedral sites, while sodium ions located in two different prismatic sites.[1]

Reference in this part:

1 S. Doubaji, M. Valvo, I. Saadoune, D. Mohammed and E. Kristina. *J. Power Sources* 2014, **266**: 275-281.

Fig. S29

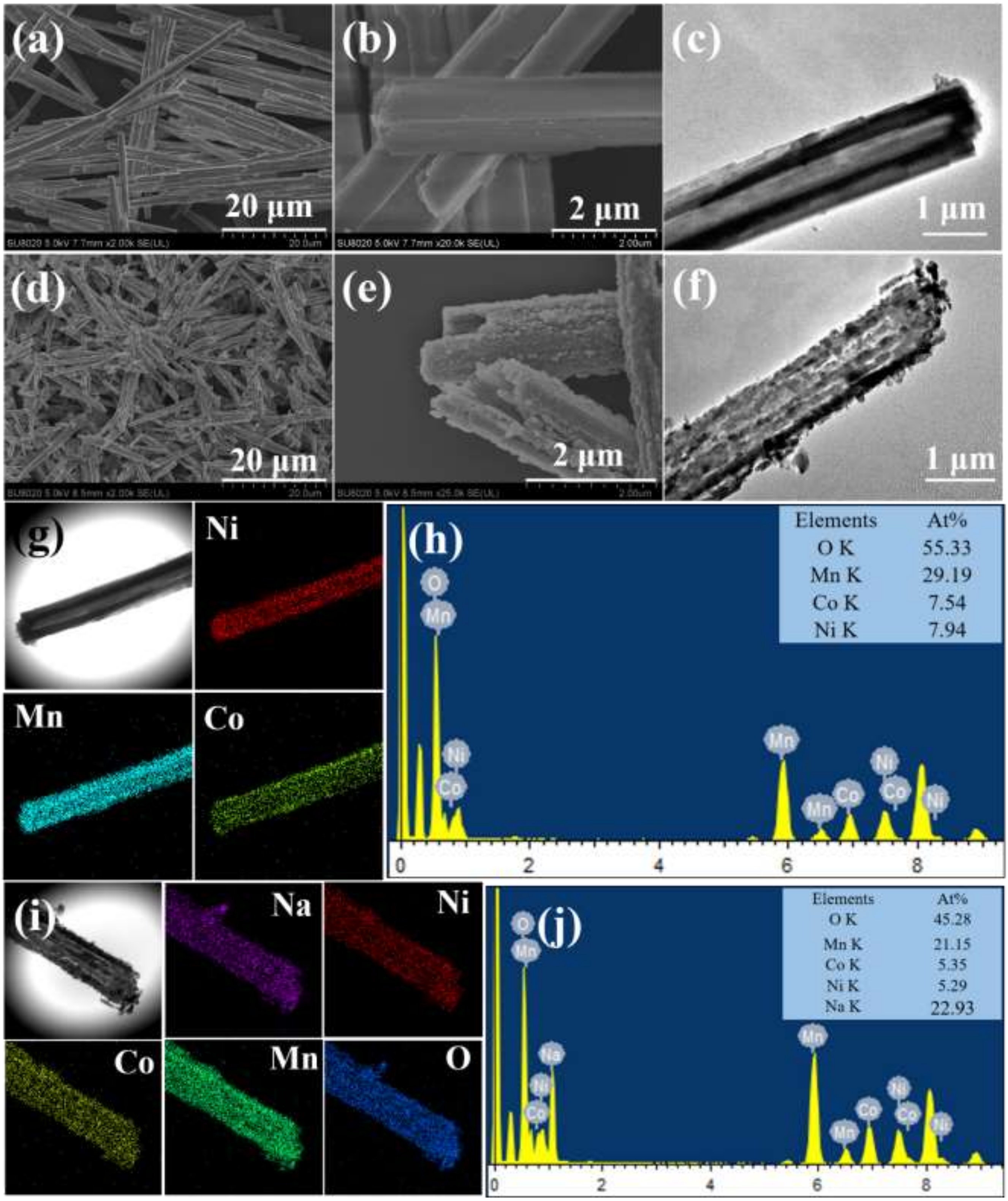

Elements	At%
O K	55.33
Mn K	29.19
Co K	7.54
Ni K	7.94

Elements	At%
O K	45.28
Mn K	21.15
Co K	5.35
Ni K	5.29
Na K	22.93

Fig. S29 (a, b) FESEM and (c) TEM images of $MC_2O_4·xH_2O$ (M= Ni, Co and Mn) precursor for $Na_{0.56}Ni_{0.13}Co_{0.13}Mn_{0.54}O_2$. (d, e) FESEM and (f) TEM images of $Na_{0.56}Ni_{0.13}Co_{0.13}Mn_{0.54}O_2$ product. (g) EDS elemental mappings (Ni, Co, Mn and O) and (h) EDS spectrum of $MC_2O_4·xH_2O$ (M= Ni, Co, Mn and O) precursor for $Na_{0.56}Ni_{0.13}Co_{0.13}Mn_{0.54}O_2$. (i) EDS elemental mappings (Na, Ni, Co, Mn and O) and (j) EDS spectrum of $Na_{0.56}Ni_{0.13}Co_{0.13}Mn_{0.54}O_2$ product.

FESEM and TEM images (Fig. S29) show that the metal oxalate precursor and $Na_{0.56}Ni_{0.13}Co_{0.13}Mn_{0.54}O_2$ product are composed of large scale of microrods with diameters of 1-2 μm and lengths over 20 μm. The hollow structures are confirmed by the TEM images in Fig. S29c and f. The diameter and length of $Na_{0.56}Ni_{0.13}Co_{0.13}Mn_{0.54}O_2$ product is smaller than that of the metal oxalate precursor due to the shrinkage and breaking during the calcination process. The element mappings of $MC_2O_4·xH_2O$ (M= Ni, Co, Mn and O) precursor for $Na_{0.56}Ni_{0.13}Co_{0.13}Mn_{0.54}O_2$ in Fig. S29g show uniform distribution of Ni, Co, Mn and O elements along the axial direction with hollow interior. The ratio of Ni, Co and Mn in Fig S29h was about 1.05:1:3.89, which is very close to the theoretical ratio (1:1:4) $MC_2O_4·xH_2O$ (M= Ni, Co, Mn and O) precursor. According to the literatures [1,2], the maximum atomic ratio of sodium to transitional metal that can be accommodated in the layered structure is 0.7 during chemical synthesis, because of the destabilization of sodium in the Na1 site in conjunction with Na2−Na2 repulsion within the sodium layer. We try to synthesize the Na-rich mixed metal oxide cathode materials $Na_{0.56}Ni_{0.13}Co_{0.13}Mn_{0.54}O_2$ in a similar way. The results in Fig. S29i indicate the uniform distribution of Na, Ni, Co and Mn elements in the $Na_{0.56}Ni_{0.13}Co_{0.13}Mn_{0.54}O_2$ along the axial direction with hollow interior and the atomic ratio is about 4.28:0.98:1:3.95 in Fig. S29j which is close to the theoretical ratio of the $Na_{0.56}Ni_{0.13}Co_{0.13}Mn_{0.54}O_2$ product (4.3:1:1:4).

References in this part:

1 M. Sathiya, J. Thomas, D. Batuk, V. Pimenta, R. Gopalan and J. M. Tarascon. *Chem. Mater.* 2017, **29**: 5948-5956.

2 Y. Lei, X. Li, L. Liu and G. Ceder. *Chem. Mater.* 2014, **26**: 5288-5296.

Fig. S30

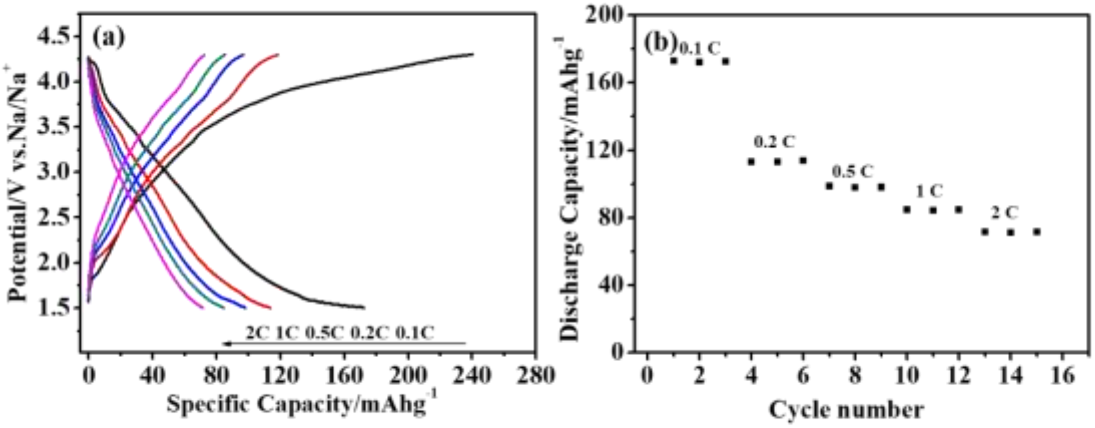

Fig. S30 Electrochemical performances of $Na_{0.56}Ni_{0.13}Co_{0.13}Mn_{0.54}O_2$ microtube. (a) Charge-discharge profiles in potential of 1.5-4.3 V at various rates., (b) Rate capability at different rates.

Electrochemical performances of the as-prepared $Na_{0.56}Ni_{0.13}Co_{0.13}Mn_{0.54}O_2$ microtube sample are shown in Fig. S30. $Na_{0.56}Ni_{0.13}Co_{0.13}Mn_{0.54}O_2$ microtubes deliver the first charging capacity of 240.2 mAh g^{-1} and discharging capacity of 172.2 mAh g^{-1} with an initial coulombic efficiency of 71.6% at 0.1 C (1 C=180 mAh g^{-1}). It achieves discharge capacities of 172.2, 112.9, 98.6, 84.7 and 71.5 mAh g^{-1} at the rates of 0.1 C, 0.2 C, 0.5 C, 1 C and 2 C, respectively. To be noted that test results of the microtube electrode materials for sodium ion battery are preliminary and further investigation is necessary.[1]

Reference in this part:

1 K. Kaliyappan, J. Liu, B. W. Xiao, A. Lushington, R. Y. Li, T. K. Sham and X. L. Sun, *Adv. Funct. Mater.* 2017, **27**: 1701870.

Table S1

Table S1 The over-potentials of LNCM811-MTs, LNCM-MPs, LR-MTs and LR-MPs at different rates, obtained from Fig. 3 and Fig. S9.

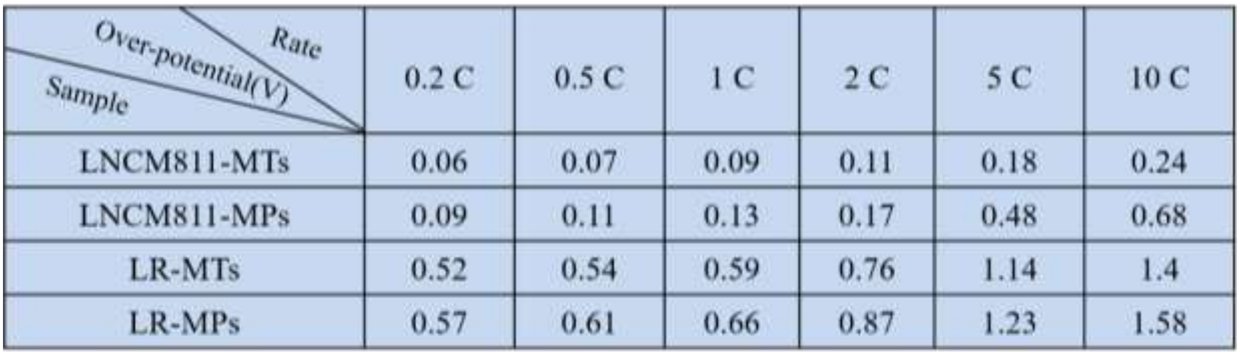

Over-potential(V) Rate Sample	0.2 C	0.5 C	1 C	2 C	5 C	10 C
LNCM811-MTs	0.06	0.07	0.09	0.11	0.18	0.24
LNCM811-MPs	0.09	0.11	0.13	0.17	0.48	0.68
LR-MTs	0.52	0.54	0.59	0.76	1.14	1.4
LR-MPs	0.57	0.61	0.66	0.87	1.23	1.58

Table S2

Table S2 The lattice parameters of LNCM811-MTs, LNCM-MPs, LR-MTs and LR-MPs obtained from Fig. S2.

Sample	a(Å)	c(Å)	c/a	$I_{(003)}/I_{(104)}$
LNCM811-MTs	3.4859	14.1669	4.0641	1.80
LNCM811-MPs	3.4859	14.1844	4.0089	1.66
LR-MTs	2.8488	14.1220	4.9572	1.82
LR-MPs	2.8217	13.0244	4.6158	1.37

As shown in Fig. S2 and Table S2, the intensity ratios of (003) and (104) peaks of LNCM811-MTs and LR-MTs are as high as 1.80 and1.82, while the intensity ratios of LNCM811-MPs and LR-MPs are 1.66 and 1.37, respectively, indicating that LNCM811-MTs and LR-MTs have less cation disorder of Li$^+$ and Ni^{2+} than LNCM811-MPs and LR-MPs. [1]

Reference in this part:

[1] T. Ohzuku, A. Ueda, M. Nagayama, Y. Iwakoshi, H. Komori, *Electrochim. Acta.* **1993**, *38*, 1159.

Table S3

Table S3 Electrochemical performance comparison between the as-prepared cathode materials and other reported results.

Electrochemical window (V)	Sample	Initial CE(%)	0.2 C (mAh g^{-1})	0.5 C (mAh g^{-1})	1 C (mAh g^{-1})	10 C (mAh g^{-1})	Ref.
2.8-4.3	LNCM811	79.18	180.2	179.4	168.1	98.3	1
3.0-4.3	LNCM811	-	182.1	175.5	169.3	103.3	2
2.8-4.3	LNCM811-MTs	83.3	194.5	180.6	171.2	139.4	This work
2.0-4.8	LR111	74.8	220.8	196.8	174.2	49	3
2.0-4.8	LR111	69.3	215.6	181.2	168.5	-	4
2.0-4.8	LR111-MTs	86.0	267.6	237.5	211.3	127.8	This work
3.0-4.5	LNCM622	-	188.3	-	173.5	125.1	5
2.8-4.7	LNCM622	73.3	182.1	170.3	147.7	86.6	6
2.8-4.3	LNCM622-MTs		185.6	179.0	168.9	139.9	This work
3.0-4.4	LNCM523	82.3	172	-	160.3	129	7
2.8-4.2	LNCM523	86.6	170.5	155.1	137.6	96.7	8
2.8-4.3	LNCM523-MTs		173.2	164.7	151.1	127.5	This work
2.7-4.3	LNCA	85.5	191.1	175.6	167.0	103.2	9
3.0-4.3	LNCA	80.3	180.7	173.2	169.6	132.3	10
2.8-4.3	LNCA-MTs		194.5	179.3	172.5	138.6	This work

Samples' Chemical formulas:

LNCM811: $LiNi_{0.8}Co_{0.1}Mn_{0.1}O_2$; LNCM811-MTs: $LiNi_{0.8}Co_{0.1}Mn_{0.1}O_2$ microtube;

LR111: $Li_{1.2}Ni_{0.13}Co_{0.13}Mn_{0.54}O_2$; LR111-MTs : $Li_{1.2}Ni_{0.13}Co_{0.13}Mn_{0.54}O_2$ microtube;

LNCM622: $LiNi_{0.6}Co_{0.2}Mn_{0.2}O_2$; LNCM622-MTs: $LiNi_{0.6}Co_{0.2}Mn_{0.2}O_2$ microtube;

LNCM523: $LiNi_{0.5}Co_{0.2}Mn_{0.3}O_2$; LNCM523-MTs: $LiNi_{0.5}Co_{0.2}Mn_{0.3}O_2$ microtube;

LNCA: $LiNi_{0.8}Co_{0.15}Al_{0.05}O_2$; LNCA-MTs: $LiNi_{0.8}Co_{0.15}Al_{0.05}O_2$ microtube;

References in this part:

1 Y. F. Su, G. Chen, L. Chen, W. K. Li, Q. Y. Zhang, Z. R. Yang, Y. Lu, L. Y. Bao, J. Tan, R. J. Chen, S. Chen, F. Wu, *ACS Appl. Mater. Interfaces* 2018, **10**, 6407-6414.

2 Q. Li, R. B. Dang, M. M. Chen, Y. L. Lee, Z. B. Hu, X. L. Xiao, *ACS Appl. Mater. Interfaces* 2018, **10**, 17850-17860.

3 F. Fu, Q. Wang, Y. P. Deng, C. H. Shen, X. X. Peng, L. Hang, S. G. Sun, *J. Mater. Chem. A* 2015, **3**, 5197-5203.

4 Y. X. Li, S. M. Li, B. H. Zhong, X. D. Guo, Z. G. Wu, W. Xiang, H. Liu, G. B. Liu, *J. Solid State Electrochem.* 2018, **22**, 547-554.

5 S. W. Li, X. T. Fu, J. W. Zhou, Y. Z. Han, P. F. Qi, X. Gao, X. Feng, B. Wang, *J. Mater. Chem. A* 2016, **4**, 5823-5827.

6 S. W. Lee, M. S. Kim, J. H. Jeong, D. H. Kim, K. Y. Chung, K. C. Roh, K. B. Kim, *J. Power Sources* 2017, **360**, 206-214.

7 Z. Y. Wang, S. S. Huang, B. J. Chen, H. Wu, Y. Zhang, *J. Mater. Chem. A* 2014, **2**,19983-19987.

8 J. Yang, Z. Y. Yu, B. Yang, H. X. Liu, J. S. Hao, T. L. Yu, K. Chen, *Electrochim. Acta* 2018, **266**, 342-347.

9 N. T. Wu, H. Wu, W. Yuan, S. J. Liu, J. Y. Liao, Y. Zhang, *J. Mater. Chem. A* 2015, **3**, 13648-13652.

10 M. Liang, D. Song, H. Z. Zhang, X. X. Shi, Q. Wang, L. Q. Zhang, *ACS Appl. Mater. Interfaces* 2017, **9**, 38567-38574.